

Optical constants of several multilayer transition metal dichalcogenides measured by spectroscopic ellipsometry in the 300–1700 nm range: high-index, anisotropy, and hyperbolicity

Battulga Munkhbat,^{1,2,*} Piotr Wróbel,^{3,*} Tomasz J. Antosiewicz,^{3,1,†} and Timur O. Shegai^{1,‡}

¹*Department of Physics, Chalmers University of Technology, SE-412 96 Gothenburg, Sweden*

²*Department of Photonics Engineering, Technical University of Denmark, 2800 Kongens Lyngby, Denmark*

³*Faculty of Physics, University of Warsaw, Pasteura 5, PL-02-093 Warsaw, Poland*

Transition metal dichalcogenides (TMDs) attract significant attention due to their exceptional optical and excitonic properties. It was understood already in the 1960s, and recently rediscovered, that many TMDs possess high refractive index and optical anisotropy, which make them attractive for nanophotonic applications. However, accurate analysis and predictions of nanooptical phenomena require knowledge of dielectric constants along both in- and out-of-plane directions and over a broad spectral range – information, which is often inaccessible or incomplete. Here, we present an experimental study of optical constants from several exfoliated TMD multilayers obtained using spectroscopic ellipsometry in the broad range of 300–1700 nm. The specific materials studied include semiconducting WS₂, WSe₂, MoS₂, MoSe₂, MoTe₂, as well as, in-plane anisotropic ReS₂, WTe₂, and metallic TaS₂, TaSe₂, and NbSe₂. The extracted parameters demonstrate high-index (n up till ≈ 4.84 for MoTe₂), significant anisotropy ($n_{\parallel} - n_{\perp} \approx 1.54$ for MoTe₂), and low absorption in the near infrared region. Moreover, metallic TMDs show potential for combined plasmonic-dielectric behavior and hyperbolicity, as their plasma frequency occurs at around ~ 1000 – 1300 nm depending on the material. The knowledge of optical constants of these materials opens new experimental and computational possibilities for further development of all-TMD nanophotonics.

I. INTRODUCTION

The recent interest in 2D semiconductors stems from the direct band gap of monolayer MoS₂.^{1,2} In addition to exciting monolayer physics, multilayer transition metal dichalcogenides (TMDs) possess a number of attractive optical properties. The prospects of multilayer TMDs for optics have been discussed already in the 1960s.³ For example, due to their van der Waals (vdW) nature, TMDs are naturally anisotropic, which is reflected in their physical and optical properties.^{4–8} Due to large oscillator strengths of electronic excitations around the A-, B- and C-exciton bands, which are stable in both mono- and multilayer forms and even at room temperature, TMD materials possess high refractive indexes in the visible and near infrared range.^{9–12} Moreover, below the A-exciton absorption band, there is a relatively broad region of low loss.^{6,10}

These observations have led to a recently renewed interest in TMD optics and nanophotonics. This interest has grown even more after a publication of several nanopatterning methods of TMDs and studies of optical phenomena in resulting TMD nanostructures.^{13,14} This includes recent observations of high-index Mie resonances and anapole states in WS₂ nanodisks,¹³ optical anisotropy in TMD slabs^{6,8} and nanocones,¹⁵ self-hybridization in TMD slabs¹⁶ and nanotubes,¹⁷ optical modes in lattices of TMD nanostructures,¹⁸ improved second-harmonic generation in WS₂ and MoS₂ disks,^{19,20} high-index metamaterials,²¹ nanoholes down to ~ 20 nm,²² and TMD metamaterials with atomically sharp edges.²³

Theoretical predictions of large values of dielectric

functions of TMDs and related vdW materials include density functional theory (DFT) studies, which confirm exceptionally high and anisotropic permittivity tensors in these materials.^{24,25} Theoretically, MoTe₂, ReS₂, and ReSe₂ compounds were predicted to have the highest values of the in-plane dielectric function. Together, these experimental observations and theoretical predictions strongly motivate further development of TMD nanophotonics. The knowledge of optical constants of these materials is essential in this regard. However, these parameters are often not precisely known, the out-of-plane values are often assumed, the response is measured within too narrow a spectral range. In addition, the quality of the extracted optical constants for a TMD material highly depends on the sample preparation,^{10,26} number of layers,^{27,28} and their lateral dimensions. The emerging field of TMD nanophotonics needs a reliable and accurate library of both in-plane and out-of-plane optical constants of various TMDs over a broad spectral range to explore their potential not only in the visible but also in the near-infrared optoelectronic applications. Here, we present such a library of TMDs which have been characterized using the same very sensitive and accurate ellipsometric approach which accounts for sample and measurement nonidealities such as surface roughness, thickness non-uniformity, as well as spectrometer bandwidth and beam angular spread, ensuring a good level of consistency between all our results.

Specifically, we have measured both in-plane and out-of-plane optical constants of high-quality mechanically-exfoliated TMDs over a broad spectral range of 300–1700 nm using spectroscopic ellipsometry. Specifically, we investigated several important multilayer TMDs with large lateral dimensions, including semiconduct-

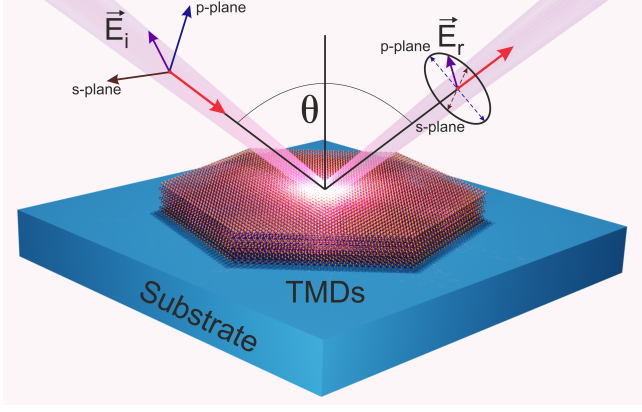


FIG. 1. Schematic of the spectroscopic ellipsometry measurements on mechanically exfoliated multilayer TMDs on a substrate.

ing WS_2 , WSe_2 , MoS_2 , MoSe_2 , MoTe_2 , as well as, in-plane anisotropic ReS_2 , WTe_2 , and metallic TaS_2 , TaSe_2 , and NbSe_2 . Our experimentally obtained data from such high-quality TMDs reveal several interesting optical properties that are promising for future nanophotonic and optoelectronic applications.

II. RESULTS AND DISCUSSION

To extract the optical constants, we prepared all multilayer TMD flakes by mechanical exfoliation directly from high quality bulk crystals (HQ-graphene) onto substrates. However, in order to perform spectroscopic ellipsometry measurements with low uncertainty, the lateral dimensions of the TMD flakes are critical, and must be larger than the beam spot during the measurements.

In this work, the spectroscopic ellipsometry measurements, see Fig. 1 for scheme, were performed using a variable angle spectroscopic ellipsometer with a Dual Rotating Compensator design (VASE Woollam RC2) equipped with focusing probes to reduce the beam diameter to $\sim 300 \mu\text{m}$. To provide multilayer TMDs of sufficient lateral dimensions, all multilayer TMD flakes were mechanically exfoliated from bulk crystals, first, onto polydimethylsiloxane (PDMS) stamps using the scotch-tape method. Subsequently, the partially transparent semiconducting flakes were transferred onto one-side polished silicon substrates with a self-limiting natural oxide layer ($\sim 1\text{-}3 \text{ nm}$) using the all-dry-transfer method²⁹ with a few important concerns.³⁰ The lossy and/or metallic TMD flakes were transferred onto silicon substrates with thermally grown SiO_2 with nominal thicknesses of $3 \mu\text{m}$ or $8.8 \mu\text{m}$. First, we chose the original bulk crystals carefully, and exfoliated multilayers onto PDMS stamps only from large (at least a centimeter) homogeneous crystals using a blue scotch-tape. Second, due to the thermoplastic properties of the PDMS film, the adhesion between the TMD flakes and PDMS slightly decreases at el-

evated temperature (here 60°C). By exploiting this property, large multilayer TMDs with relatively homogeneous thickness can be readily transferred onto a substrate for ellipsometric measurements. Thicknesses of the transferred TMD flakes were measured using a VEECO profilometer. For our study, we chose multilayer TMDs with thicknesses ranging from a few tens of nanometers to several microns. Exemplary TMD flakes are shown in Fig. 2. These include semiconducting WS_2 , WSe_2 , MoS_2 , MoSe_2 , MoTe_2 , as well as, bianisotropic ReS_2 , WTe_2 , and metallic TaS_2 , TaSe_2 , and NbSe_2 , which are among the most promising TMDs for future nanophotonic and optoelectronic applications. After sample preparation, we performed spectroscopic ellipsometry measurements and analysis for all freshly prepared multilayers in a broad spectral range of $300\text{--}1700 \text{ nm}$ in steps of 1 nm . The measurements were performed at multiple angles of incidence ranging from 20° to 75° in steps of 5° , although for some flakes the maximum angle was reduced to ensure that the illumination spot was smaller than a TMD flake. The obtained dielectric tensor components data as a function of wavelength for all studied materials are provided in the Supporting Information (SI).

A. Uniaxial semiconductors

We begin our study by investigating multilayers of uniaxial TMD semiconductors, such as MoS_2 , MoSe_2 , MoTe_2 , WS_2 , and WSe_2 . These are one of the most well-studied TMD materials, especially in relation to their monolayers² and vdW heterostructures.³¹ Recently, they have been also suggested as promising high-index dielectric material platform for future nanophotonics.^{9,13,25,32,33} Here, we report both their in-plane and out-of-plane dielectric constants and compare our results to previously reported parameters.^{8,9,24,25,34,35} Their permittivities (both real and imaginary parts) were measured utilizing the ellipsometry technique whose basic principle is depicted in Fig. 1. In general, ellipsometry measures changes of the polarization state of light upon reflection of an incident beam from a sample. The change is represented by two measured parameters Ψ (Psi) and Δ (Delta), which correspond to the ratio of the reflection coefficients and the phase difference between the p - and s -polarization components of the incident beam. The described above approach assumes that no change of polarization state occurs upon reflection from the sample. In the case of anisotropic samples, cross-polarization might occur, thus more complex analysis including General Ellipsometry or Mueller Matrix ellipsometry are required to address this issue. However, in the case of uniaxial anisotropic materials proper sample alignment results in canceling all the off-diagonal components of the Mueller Matrix which simplifies the procedure to the standard ellipsometry. While this alignment is straightforward for TMD flakes due to their vdW nature, which dictates the alignment

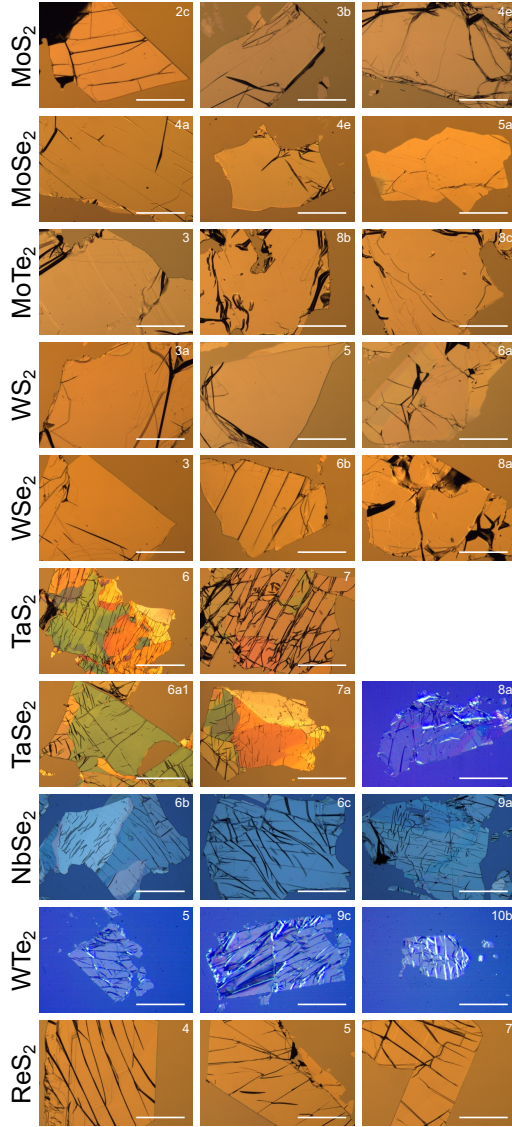


FIG. 2. Exemplary images of exfoliated TMD flakes used ellipsometric measurements. First five rows show uniaxial semiconducting TMD flakes: MoS₂, MoSe₂, (2H)MoTe₂, WS₂, and WSe₂, respectively. Next three rows contain uniaxial metallic TMD flakes: TaS₂, TaSe₂, and NbSe₂. The last two rows contain the two characterised biaxial TMD flakes: metallic (though in the optical range the permittivity is positive) WTe₂ and semiconducting ReS₂, respectively. All semiconducting TMD flakes were placed directly on a Si substrate with a rough (diffusive) backside. In the case of metallic TMDs a thermally oxidized Si substrate was used (with SiO₂ thickness of 3 μ m or 8.8 μ m). The scale bar is 300 μ m long and the same in every panel.

of the crystalline axes, the full Mueller Matrix was measured to ensure this proper alignment (Fig. S1–Fig. S10).

To extract physical parameters like thickness or complex refractive index of a given material, an appropriate model describing the investigated structure has to be built. Parameters of interest are extracted by a simultaneous fit of the model parameters to the Psi and

Delta curves. Although the technique allows for optical characterization of a sample with thickness down to a monolayer, measurements of the anisotropic samples are challenging³⁶ and require thick samples to assure sufficient light interaction with in-plane and, especially, out-of-plane polarization components to sense the anisotropy. That is particularly difficult for samples with a high refractive index what reduces greatly the angle of refraction and thus the amount of the out-of-plane components of the refracted beam in the sample. This problem can be partially overcome by using an appropriate scheme of measurements and analysis that allows improving the sensitivity of the model (see Methods).

In our experiment, the samples exhibiting transparency in the visible-near infrared (VIS-NIR) range are in the form of thick TMDs layers (from a few tens of nm to a few microns) exfoliated onto roughened Si substrates with a native SiO₂ layer. In the extraction procedure, we use a multisample analysis approach with the model containing a semi-infinite Si substrate with a native oxide and thin layer of a TMDs. The optical constants of Si and SiO₂ are taken from the CompleteEASE database and their validity was confirmed by reference measurements of substrates next to the TMD flakes. The in-plane component of the complex refractive index is described by multiple Tauc-Lorentz dispersion model terms, while the out-of-plane component is described by a single pole described by ϵ_∞ and its ultraviolet (UV) position and amplitude (see Methods). In the analysis, both surface roughness and layer nonuniformity are taken into account and the goodness of fit parameter, defined as the mean squared error (MSE), is minimized during the fitting procedure. The sensitivity of the technique to the anisotropic properties of the samples can be deduced from the asymmetry of the interference maxima in the Ψ curves occurring in the transparent regions of the samples. Moreover, a significant drop of MSE when the permittivity model is changed from isotropic to anisotropic indicates that this approach allows for extracting the out-of-plane component. Fig. 3 shows the complex permittivities of the analyzed uniaxial semitransparent TMDs (see Fig. S11–Fig. S15 for quality of the fits to Ψ and Δ). The surface of some of the samples is nonuniform, cf. Fig. 2, with wrinkles/folds and atomic steps that cannot be easily subsumed into roughness within the model. Since the surface features influence the UV region the most, to minimize the uncertainty of the extracted dispersion curves we consider the data from 300 nm.

Extracted in-plane (n_{\parallel} , here $n_{\parallel} = \sqrt{\epsilon_{xx}} = \sqrt{\epsilon_{yy}}$) and out-of-plane ($n_{\perp} = \sqrt{\epsilon_{zz}}$) refractive indices at 1550 nm for semiconducting TMDs and their optical anisotropy (Δn) are displayed in Fig. 4. Overall, multilayer TMDs exhibit higher refractive indices at 1550 nm, in contrast to conventional semiconductors, e.g., c-Si (~ 3.47),³⁷ a-Si (~ 3.48),³⁸ and GaAs (~ 3.37).³⁹ Our data in Fig. 4a reveal a few interesting trends. First, we observe higher index values among Mo-based TMDs, ~ 4.07 (MoS₂), ~ 4.21 (MoSe₂), and ~ 4.84 (MoTe₂), when compared to other

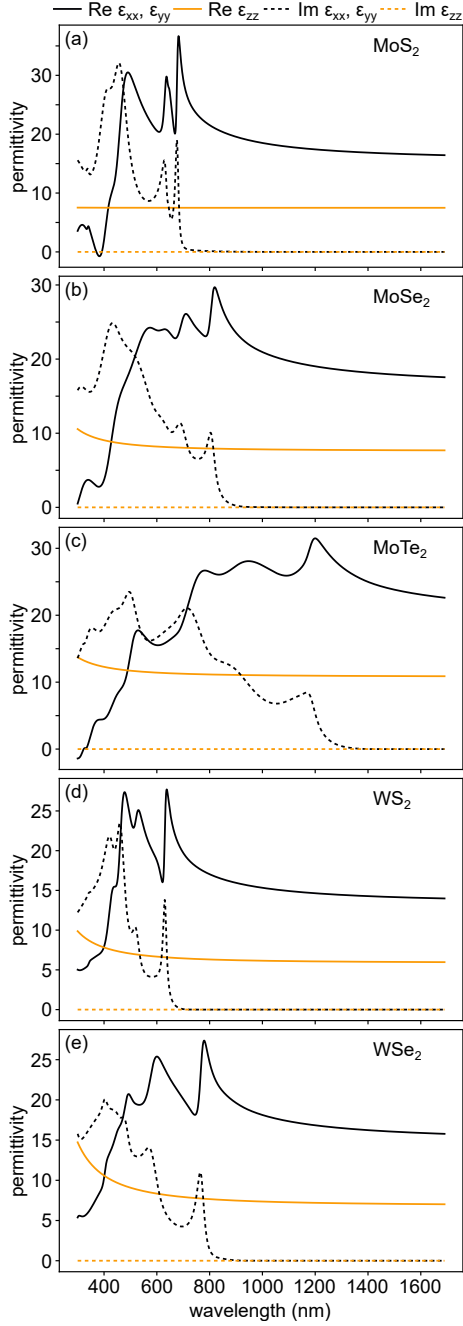


FIG. 3. Permittivity of uniaxial semiconducting TMD flakes: (a) MoS₂, (b) MoSe₂, (c) MoTe₂, (d) WS₂, and (e) WSe₂. Corresponding exemplary Mueller Matrix measurements proving their uniaxial nature are plotted in Fig. S1–Fig. S5.

W-based WS₂ (~ 3.75), and WSe₂ (~ 3.99) semiconducting TMDs. Second, these data also reveal that the refractive index increases depending on the chalcogen atom of TMDs in the following order: $n_{\text{MoS}_2} < n_{\text{MoSe}_2} < n_{\text{MoTe}_2}$. This observation agrees well with theoretically predicted results from an earlier DFT study.²⁴ In parallel to high index, it is worth mentioning that their optical loss in

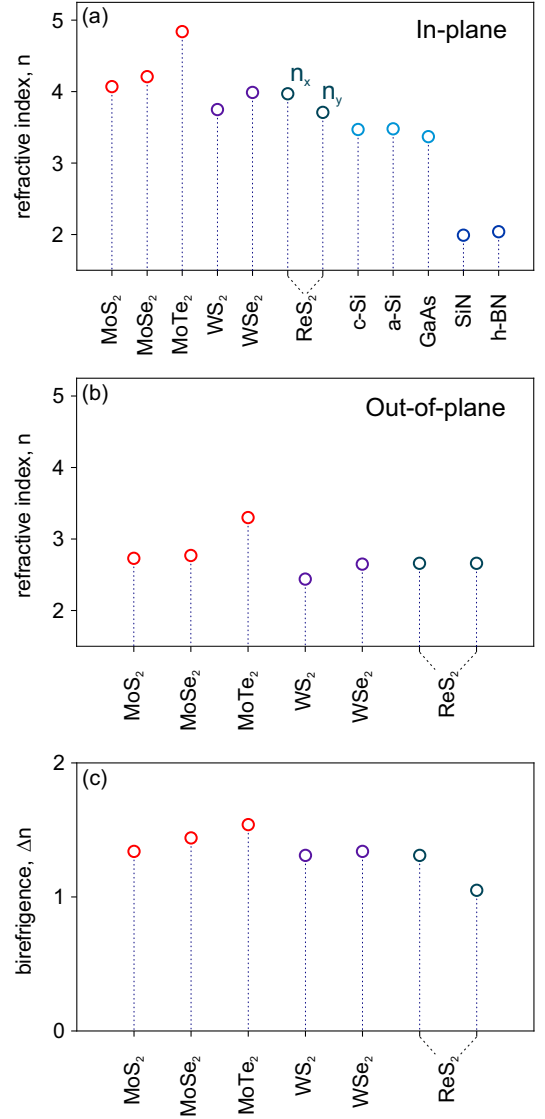


FIG. 4. Comparison of extracted refractive indices of common TMDs at the Telecom C band (1550 nm) with conventional semiconductors. (a) In-plane refractive index, (b) out-of-plane refractive index, (c) birefringence.

the near-infrared range is negligibly small judging from their very small imaginary part of the permittivities, cf. Fig. 3. This property opens a possibility of using multilayer TMDs for low-loss nanophotonics applications.^{33,40}

Another interesting optical feature in multilayer TMDs is their anisotropic properties due to vdW stacking nature, which results in large birefringence. Fig. 4c shows that TMDs exhibit relatively large birefringence of $\Delta n \geq 1.3$ due to their lower out-of-plane refractive indices ranging from n_{\perp} : 2.44 (WS₂) to 3.3 (MoTe₂), in contrast to their in-plane indices (cf. Fig. 4ab). MoTe₂ shows the largest birefringence of $\Delta n \sim 1.54$ among uniaxial semiconducting TMDs, whereas other materials MoS₂, MoSe₂, WS₂, and WSe₂ exhibit birefringence values of $\Delta n \sim 1.34$, ~ 1.44 , ~ 1.31 , and ~ 1.34 , respectively. It

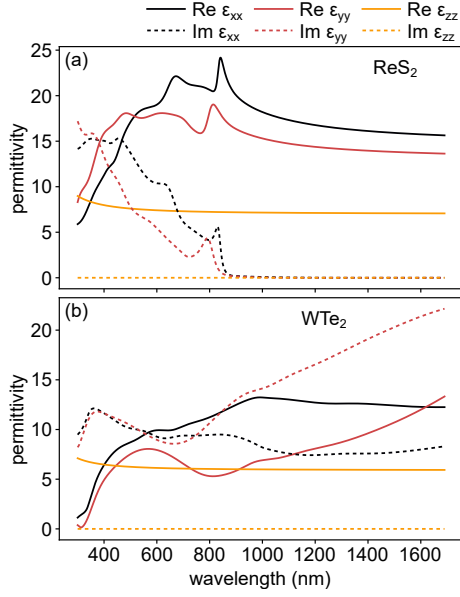


FIG. 5. Permittivity of bianisotropic materials: (a) semiconducting ReS₂ and (b) lossy (metallic at low frequencies) WTe₂ TMD flakes. Corresponding exemplary Mueller Matrix measurements in Fig. S7 and Fig. S6 show their biaxial nature.

should be noted that the obtained birefringence values in TMDs are 7-8 times larger than other anisotropic materials, e.g., yttrium orthovanadate and rutile TiO₂, which exhibit typically smaller anisotropy of $\Delta n \sim 0.2 - 0.3$.⁴¹ Our data are in a good agreement with previous both experimental and theoretical reports.^{6,8,24} For instance, our result for MoS₂: $\Delta n \sim 1.34$ at 1550 nm is in agreement with previously obtained experimental values of $\Delta n \sim 1.4$ (at 1530 nm, extracted by scattering scanning near-field optical microscopy (s-SNOM)⁶) and $\Delta n \sim 1.5$ (in the infrared, extracted by spectroscopic ellipsometry⁸). However, due to the lack of reported birefringence data for a broader range of available TMDs, it is difficult to perform a comprehensive comparison. Our study partially fills this gap and, thus, provides an important contribution to the database of TMD optical constants, useful for the development of future all-TMD nanophotonic applications. Additionally, a combination of high-index ($n \gtrsim 4$), low-loss and large birefringence ($\Delta n \gtrsim 1.4$) in the near-infrared range makes multilayer TMDs a promising material platform for exploring photonic surface waves e.g., Dyakonov^{42,43} and Zenneck⁷ surface waves.

B. Biaxial semiconductor

We now turn to the biaxial semiconductor – ReS₂. The in-plane anisotropy of this material stems from the formation of covalent Re-Re bonds and correspondingly the 1T'-phase it adopts.⁴⁴ This material has recently been theoretically predicted to have one of the high-

est permittivities in the visible – near-infrared spectral range.²⁵ Here, we report its experimentally measured optical constants. Performing ellipsometry on such a material is more challenging than for uniaxial TMDs from the measurement as well as analysis perspective. In-plane anisotropy requires rotation of the sample during the measurement to extract Euler angles of the material's crystallographic structure. This, in turn, requires that the lateral size of a ReS₂ flake should be larger than the beam spot for all in-plane directions. However, due to in-plane anisotropy ReS₂ tends to shear-off along the *b*-axis⁴⁵ what makes exfoliation of a large symmetric flake extremely difficult. We were, however, able to prepare relatively large ReS₂ samples with some folds which do not interfere with our measurements (Fig. 2). Moreover, interaction of polarized light with such a sample leads to a cross-polarization effect, thus Ψ and Δ lose their meaning and the Generalized Ellipsometry, or more general Mueller Matrix ellipsometry, is required. To ensure sensitivity of the methods both to in-plane and out-of-plane components we performed a multisample analysis with thicknesses ranging from 200 nm to approximately 600 nm and at least two rotation angles with other measurement parameters being the same as for uniaxial semiconducting TMDs above. It is worth mentioning that due to problems with exfoliation some of the ReS₂ flakes are characterized by a terrace-like surface morphology and are not uniform in thickness. Thus in the analysis, data acquired for each rotation angle are treated as for a separate sample and its thickness (for every in-plane rotation angle) is a free fitting parameter. However, despite the presence of terraces, the crystalline axes of each flake are not disturbed and thus the fitted orientation (in-plane rotation) angles are consistent with the rotation angles during measurements. The in-plane permittivities ϵ_{xx} and ϵ_{yy} are described by multiple Tauc-Lorentz dispersion models, while the out-of-plane component is described by a single pole. The experimentally obtained permittivity for ReS₂ is shown in Fig. 5a, while the fidelity of the fits is in Fig. S17.

Here we extracted two n_{\parallel} and n_{\perp} refractive indices of ReS₂ at 1550 nm from the experimentally obtained permittivity, which yielded $n_{\parallel,xx}$: 3.97, $n_{\parallel,yy}$: 3.71, and n_{\perp} : 2.66, respectively (Fig. 4a,b). ReS₂ exhibits birefringence values of $\Delta n_{xx} - n_{zz} \sim 1.31$ and $\Delta n_{yy} - n_{zz} \sim 1.05$ (Fig. 4c). The obtained $\Delta n_{yy} - n_{zz} \sim 1.05$ (ReS₂) is smaller than other TMDs. However, our data shows that ReS₂ possess in-plane birefringence of Δn_{xx-yy} : ~ 0.26 at 1550 nm, in addition to its out-of-plane anisotropy. This suggests that ReS₂ could be an interesting material for next-generation photonics due to its both in-plane and out-of-plane anisotropic properties ($\text{Re}(\epsilon_{xx}) \neq \text{Re}(\epsilon_{yy}) \neq \text{Re}(\epsilon_{zz}) \neq \text{Re}(\epsilon_{xx})$), together with high-index (≥ 3.7) and low-loss at telecom range. Moreover, a recent study⁴⁶ reports a light-induced phase transition in mono- and bilayers of ReS₂, which could be an additional benefit for ReS₂-based nanophotonic applications.

C. Metallic and Hyperbolic (Uniaxial and Biaxial)

The third group of samples investigated in the experiment are TMDs that exhibit absorption in the whole measured wavelength range that comes from the metallic response and/or additional interband transitions. Due to a lack of sharp features in Ψ and Δ spectra when placed directly on a reflective substrate, they require a special scheme of measurements to assure sufficient interaction of light with the samples and uniqueness of the ellipsometric models. This additional requirement is obtained by using a few-micron-thick thermally grown SiO_2 layer on top of a Si substrate. When a thin semitransparent absorbing TMD flake is deposited on such a support, interference in the SiO_2 layer yields a distinct modulation of the ellipsometric signal, whose contrast depends on the thickness and extinction coefficient of the TMD layer. This so-called interference approach was introduced by Hilfiker *et al.*⁴⁷ showing great improvement in the sensitivity of ellipsometric models applied to absorbing materials.

In our experiment semitransparent flakes of thickness from ~ 50 nm to ~ 400 nm were exfoliated onto a $3\ \mu\text{m}$ or $8\ \mu\text{m}$ thick thermally grown SiO_2 layer on a Si substrate. The measurements with the use of standard ellipsometry were carried out for the same wavelength and incidence angle range as for the previous samples (*cf.* Fig. S8–Fig. S10 for Mueller matrix measurements confirming appropriate alignment of the uniaxial samples). In the case of bianisotropic WTe_2 the significant difference with respect to the details above was the need to perform in-plane rotation of the sample identically to ReS_2 . The anisotropic materials were modeled with Tauc-Lorentz and as needed Drude functions both for in-plane and out-of-plane components. The fitting procedure for these two types of materials is described in the Methods section.

We now study uniaxial metallic TMDs, e.g. TaS_2 , TaSe_2 , and NbSe_2 , whose permittivities obtained in our measurements are shown in Fig. 6. Interestingly, the materials exhibit both dielectric and metallic responses in the studied spectral range, as indicated by a change of the sign of the values of the in-plane $\text{Re}(\epsilon)$ from positive to negative around 1100 nm to 1400 nm, depending on the material. Specifically, the plasma frequencies of the in-plane $\text{Re}(\epsilon)$ of Ta-based TMDs TaS_2 and TaSe_2 are, respectively, at ~ 1110 nm (~ 1.11 eV) and ~ 1217 nm (~ 1.01 eV), as illustrated in Fig. 6a,b. However, their out-of-plane $\text{Re}(\epsilon_{zz})$ remain positive showing only a dielectric response over the entire studied spectral range.

On the other hand, Fig. 6c shows that both in-plane and out-of-plane components of $\text{Re}(\epsilon)$ of NbSe_2 are positive for wavelengths shorter than ~ 1390 nm, suggesting that NbSe_2 may behave like an out-of-plane anisotropic dielectric in the visible spectrum. Conversely, the real parts of the diagonal dielectric tensor become negative at longer wavelengths and retain the sign until the end of our measurement range. Furthermore, above ~ 1200 nm NbSe_2 is only weakly anisotropic. The negative sign of the in-plane dielectric function is associated with a free-

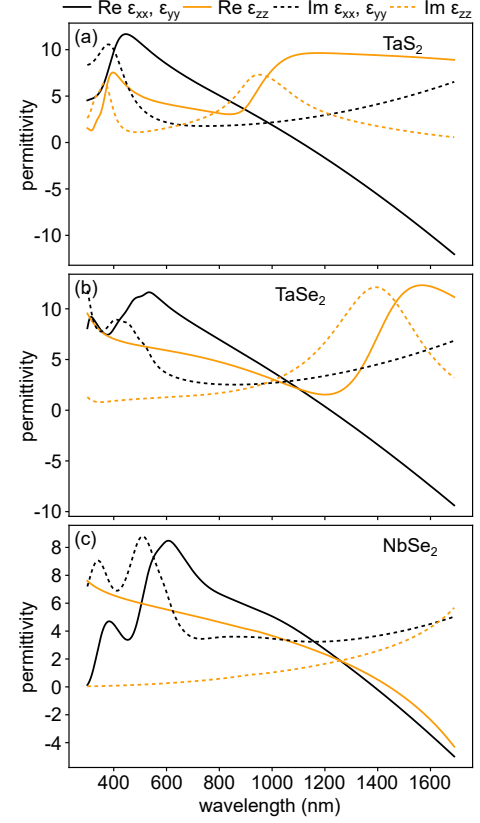


FIG. 6. Permittivity of uniaxial metallic TMD flakes: (a) TaS_2 , (b) TaSe_2 , and (c) NbSe_2 . See Fig. S8–Fig. S10 for Mueller Matrix measurements confirming their uniaxial properties and proper alignment.

electron response just like for Ta-based metallic TMDs and indicates an in-plane plasma frequency of ~ 0.89 eV. However, the negative dielectric function in the out-of-plane direction is not associated with a free-electron, Drude-like response. Rather it is due to a high oscillator strength of a Lorentz-like response, which leads to the appearance of a Reststrahlen band for wavelengths above ~ 1200 nm. The out-of-plane dielectric function should therefore become positive again at even longer wavelengths, however, this occurs outside of our measurement range (>1700 nm).

In contrast to the above three materials, WTe_2 is an in-plane anisotropic TMDs like ReS_2 , but is metallic and hyperbolic. Recently, hyperbolic dispersion in WTe_2 was demonstrated experimentally in the infrared region ($\sim 500\ \text{cm}^{-1}$) using far-field absorption measurements.⁴⁸ Later, a new hyperbolic regime in the near-infrared (~ 1 eV) was theoretically predicted in monolayer WTe_2 due to band-nested anisotropic interband transitions.⁴⁹ However, such hyperbolicity of WTe_2 in the near-infrared becomes weaker and disappears as the layer number increases from monolayer to bulk. Indeed, Fig. 5b shows the experimentally here-obtained permittivity from multilayer WTe_2 . As expected, the real part of permittivity $\text{Re}(\epsilon)$ shows no sign of hyperbolic behavior in the stud-

ied spectral range. However, we observed an interesting anisotropic behavior in the narrow spectral region around 800 nm, where $\text{Re}(\varepsilon_{xx}) > \text{Re}(\varepsilon_{zz}) > \text{Re}(\varepsilon_{yy})$. This is not a common behavior in other TMDs. Moreover, WTe_2 possesses relatively large in-plane birefringence ranging from Δn_{x-y} : ~ 0.2 (at 510 nm) to ~ 1.12 (at 880 nm). The maximum obtained $\Delta n_{x-y} \sim 1.12$ (WTe_2) is larger than a previously observed value of in-plane birefringence in ReS_2 (~ 0.26). Such large in-plane anisotropy may open new possibilities for nanophotonics, even though the imaginary part $\text{Im}(\varepsilon_{xx})$ is relatively large.

III. CONCLUSION

In conclusion, we have experimentally measured both in-plane and out-of-plane optical constants from mechanically exfoliated TMDs multilayers using spectroscopic ellipsometry over a broad spectral range of 300 nm – 1700 nm. Our measurements include several semiconducting WS_2 , WSe_2 , MoS_2 , MoSe_2 , MoTe_2 , as well as, in-plane anisotropic ReS_2 , WTe_2 , and metallic TaS_2 , TaSe_2 , and NbSe_2 materials. The extracted parameters demonstrate a combination of several remarkable optical properties, such as a high-index (n up till ~ 4.84 for MoTe_2), significant anisotropy ($n_{\parallel} - n_{\perp} \approx 1.54$ for MoTe_2), and low absorption in the near infrared region. Moreover, metallic TMDs show potential for a combined plasmonic-dielectric behavior and hyperbolicity, as their plasma frequencies occur in the $\sim 1000 - 1300$ nm range depending on the material. The knowledge of dispersive and anisotropic optical constants of these vdW materials opens new possibilities for future development of all-TMDs nanophotonics.

IV. METHODS

Sample preparation: All TMD flakes, including semiconducting and uniaxial WS_2 , WSe_2 , MoS_2 , MoSe_2 , $(2\text{H})\text{MoTe}_2$, hyperbolic and metallic $(2\text{H})\text{TaS}_2$, TaSe_2 , NbSe_2 , and biaxial ReS_2 and WTe_2 , were mechanically exfoliated from bulk crystals (HQ-graphene) onto polydimethylsiloxane (PDMS) stamps using the scotch-tape method, and then transferred onto substrates using the all-dry transfer method.^{29,30} For spectroscopic ellipsometry measurements, the lateral dimensions of the TMD flakes should be larger than the beam size. To achieve proper sizes of TMD flakes, we modified the previously developed method with few important concerns.

First, we chose the starting bulk crystals carefully, and exfoliate multilayers onto PDMS stamps only from large crystals (a centimeter at the least) with a homogeneous surface using a blue scotch-tape. Second, due to the thermoplastic properties of the PDMS film, adhesion between TMD flakes and PDMS slightly decreases at the elevated temperature of 60 °C. By exploiting this advantage, large multilayer TMDs with relatively homo-

geneous thicknesses can be easily transferred onto a substrate for ellipsometric measurements. Thicknesses of the transferred TMD flakes were measured using a VEECO profilometer, and we chose multilayer TMDs with thicknesses ranging from a few tens of nanometers to microns. The minimum lateral size of uniaxial TMD flakes investigated in this study is at least $300\text{ }\mu\text{m}$ in one direction (beam width) and at least $700\text{ }\mu\text{m}$ in the other to facilitate measurement at angles of incidence of up to (at the minimum of) 65 °. In the case of biaxial TMDs, ReS_2 and WTe_2 , both orthogonal in-plane directions need to be not smaller than $400\text{ }\mu\text{m}$ to enable measurements up to (at least) 45 °, larger if possible. For ellipsometric measurements of semiconducting TMDs, one-side polished silicon substrates with a self-limiting natural oxide layer (1-3 nm) were used. In contrast to clear sharp excitonic features of the semiconducting, metallic TMDs lack such sharp features in Ψ and Δ spectra. In order to perform high-quality measurements of metallic TMDs and to produce sharp interference features in the ellipsometric spectra, semitransparent metallic TMD flakes of TaS_2 , TaSe_2 , NbSe_2 , and WTe_2 were transferred onto silicon substrates with a $3\text{ }\mu\text{m}$ or $8.8\text{ }\mu\text{m}$ thick thermally grown SiO_2 layer.

Variable-angle spectroscopic ellipsometry: Ellipsometric measurements were carried out with the use of a Woollam RC2 dual rotating compensator (DRC) ellipsometer with a vertical auto angle stage. It allows for measurement of the full Mueller Matrix which is essential for analysis of bianisotropic samples and helpful for verifying that the uniaxial samples are correctly set up in the ellipsometer's coordinates. Another feature that is accessible in the DRC architecture is the depolarization factor which allows for measurement and modeling of a sample's nonidealities like thickness nonuniformity or influence of a device's parameters/limitations like detector bandwidth or angular spread of the beam. Due to the small lateral dimensions of TMD flakes they are measured with the use of focusing probes which reduce the light beam to a $300\text{ }\mu\text{m}$ spot at normal incidence. The configuration of the ellipsometer with mounted focusing probes does not allow for transmission measurements, thus samples were prepared and measured in reflection up to a wavelength of 1690 nm and the full accessible angle range from 20° to 75° depending of the size of the TMD flake. Modeling and fitting were done with the use of CompleteEASE v6.61.

Fitting of ellipsometric data: The investigated samples exhibit three types of optical responses which require different strategies in building appropriate models. The Ψ curves of uniaxial semitransparent TMD flakes exhibit interference maxima in the transparent regions. Proper fitting in these spectral ranges determines with very good accuracy both the thickness and the real part of the dielectric function, yielding a good starting point for further modelling of the data in the remaining spectral regions. For this type of samples we proceeded as follows:

- In the first step, an isotropic model is used and the transparent region is described by a Cauchy model $A + B/\lambda^2$, where the its parameters such as layer thickness, A and B are extracted by the Levenberg–Marquardt algorithm after fitting the model to the Ψ and Δ curves.
- In the next step, the Cauchy model is converted to the Kramers-Kronig consistent B-spline curves with their subsequent expansion to the whole wavelength range. The B-spline function approximates the fitting curves with basic functions with their argument (photon energy, eV) equally spaced. We used a 0.05 eV step in the whole energy range except where Ψ exhibits sharp or anomalous behavior corresponding to e.g. exciton bands in the dielectric function.
- In the third step, the isotropic model is converted to an anisotropic one and the out-of-plane component is described by a single UV pole. After minimization of the MSE, the B-spline model is parametrized by a General Oscillator model with the use of Tauc-Lorentz oscillators.
- The whole procedure is initially done for the thickest samples and after parametrization, the fitting procedure is repeated in a multisample analysis leading to a complex diagonal permittivity tensor which is common for all the samples.

The lack of a transparent region for the metallic TMD samples necessitates some changes to the above described procedure. First of all use of the interference approach requires a more complicated model taking into account the transparent interference layer as well as the additional interlayer present at Si and SiO₂ interface. The Si substrate with thermal SiO₂ was characterized prior to the final measurements and their extracted parameters were fixed in the initial stage of modeling.

- The first step consists of fitting an isotropic Kramers-Kronig consistent Bi-spline function to the data for the thinnest samples exhibiting the most pronounced interference maxima. The thickness of the TMDs is fixed during the fitting procedure and their values are taken from profilometric measurements.
- In the next step, the isotropic model is converted to an anisotropic one and the fitting procedure is repeated. For final improvement of the results rough-

ness as well as sample and machine nonidealities are taken into account.

- In the last step the multisample analysis is carried out and the final Bi-spline model is parametrized with Tauc-Lorentz and Drude functions.

Evaluation of the models is based on minimization of the MSE, the Correlation Matrix, and the Uniqueness test. In case of bianisotropic samples the first and second procedures was used for, respectively, ReS₂ and WTe₂ with a modification that involved using a biaxial model instead of an uniaxial.

ASSOCIATED CONTENT

Supporting Information

The Supporting Information is available free of charge at <https://pubs.acs.org/doi/10.1021/acsp Photonics>.

SI Figures S1-S10 – Exemplary Mueller Matrices for all materials; S11-S20 – Agreement between measurements and fitted models. Tables S1 and S2 – Summary of other fitting parameters; Note S1 – Uncertainty of optical parameters accompanied by Figures S21-S23.

FUNDING

B.M. and T.O.S. acknowledge financial support from the Swedish Research Council (under VR Miljö project, grant No: 2016-06059) and the Knut and Alice Wallenberg Foundation (grant No: 2019.0140). B.M. also acknowledges the European Research Council (ERC-CoG “Unity”, Grant No: 865230). P.W. and T.J.A. thank the Polish National Science Center for support via the project 2019/34/E/ST3/00359 (T.J.A.) and 2019/35/B/ST5/02477 (P.W.).

NOTES

The authors declare no competing financial interest.

Data availability: The raw ellipsometric data along with fitted models in both the proprietary format of the CompleteEASE software (Woolam) and as plain text files as well as plain text files with fitted permittivities are available at <https://doi.org/10.5281/zenodo.6205431>.

* Contributed equally to this work

† tomasz.antosiewicz@fuw.edu.pl

‡ timurs@chalmers.se

¹ Andrea Splendiani, Liang Sun, Yuanbo Zhang, Tianshu Li, Jonghwan Kim, Chi-Yung Chim, Giulia Galli, and Feng

Wang, “Emerging photoluminescence in monolayer MoS₂,” *Nano Lett.* **10**, 1271–1275 (2010).

² Kin Fai Mak, Changgu Lee, James Hone, Jie Shan, and Tony F Heinz, “Atomically thin MoS₂: a new direct-gap semiconductor,” *Phys. Rev. Lett.* **105**, 136805 (2010).

- ³ J. A. Wilson and A. D. Yoffe, “The transition metal dichalcogenides discussion and interpretation of the observed optical, electrical and structural properties,” *Adv. Phys.* **18**, 193–335 (1969).
- ⁴ Z Fei, ME Scott, DJ Gosztola, JJ Foley IV, J Yan, DG Mandrus, H Wen, P Zhou, DW Zhang, Y Sun, *et al.*, “Nano-optical imaging of WSe₂ waveguide modes revealing light-exciton interactions,” *Phys. Rev. B* **94**, 081402 (2016).
- ⁵ F Hu, Y Luan, ME Scott, J Yan, DG Mandrus, X Xu, and Z Fei, “Imaging exciton–polariton transport in MoSe₂ waveguides,” *Nat. Photonics* **11**, 356–360 (2017).
- ⁶ Debo Hu, Xiaoxia Yang, Chi Li, Ruina Liu, Ziheng Yao, Hai Hu, Stephanie N Gilbert Corder, Jianing Chen, Zhipei Sun, Mengkun Liu, and Quing Dai, “Probing optical anisotropy of nanometer-thin van der Waals microcrystals by near-field imaging,” *Nat. Commun.* **8**, 1471 (2017).
- ⁷ Viktoriia E Babicheva, Sampath Gamage, Li Zhen, Stephen B Cronin, Vladislav S Yakovlev, and Yohannes Abate, “Near-field surface waves in few-layer MoS₂,” *ACS Photonics* **5**, 2106–2112 (2018).
- ⁸ GA Ermolaev, DV Grudin, YV Stebunov, Kirill V Voronin, VG Kravets, Jiahua Duan, AB Mazitov, GI Tselikov, Andrei Bylinkin, DI Yakubovsky, *et al.*, “Giant optical anisotropy in transition metal dichalcogenides for next-generation photonics,” *Nat. Commun.* **12**, 854 (2021).
- ⁹ Yilei Li, Alexey Chernikov, Xian Zhang, Albert Rigosi, Heather M Hill, Arend M Van Der Zande, Daniel A Chenet, En-Min Shih, James Hone, and Tony F Heinz, “Measurement of the optical dielectric function of monolayer transition-metal dichalcogenides: MoS₂, MoSe₂, WS₂, and WSe₂,” *Phys. Rev. B* **90**, 205422 (2014).
- ¹⁰ Georgy A Ermolaev, Yury V Stebunov, Andrey A Vyshnevyy, Dmitry E Tatarkin, Dmitry I Yakubovsky, Sergey M Novikov, Denis G Baranov, Timur Shegai, Alexey Y Nikitin, Aleksey V Arsenin, *et al.*, “Broadband optical properties of monolayer and bulk MoS₂,” *npj 2D Mater. and Appl.* **4**, 21 (2020).
- ¹¹ Wei Li, A Glen Birdwell, Matin Amani, Robert A Burke, Xi Ling, Yi-Hsien Lee, Xuelei Liang, Lianmao Peng, Curt A Richter, Jing Kong, *et al.*, “Broadband optical properties of large-area monolayer CVD molybdenum disulfide,” *Phys. Rev. B* **90**, 195434 (2014).
- ¹² Chanyoung Yim, Maria O’Brien, Niall McEvoy, Sinéad Winters, Inam Mirza, James G Lunney, and Georg S Duesberg, “Investigation of the optical properties of MoS₂ thin films using spectroscopic ellipsometry,” *Appl. Phys. Lett.* **104**, 103114 (2014).
- ¹³ Ruggero Verre, Denis G Baranov, Battulga Munkhbat, Jorge Cuadra, Mikael Käll, and Timur Shegai, “Transition metal dichalcogenide nanodisks as high-index dielectric Mie nanoresonators,” *Nat. Nanotechnol.* **14**, 679–683 (2019).
- ¹⁴ Xingwang Zhang, Chawina De-Eknamkul, Jie Gu, Alexandra L Boehmke, Vinod M Menon, Jacob Khurgin, and Ertugrul Cubukcu, “Guiding of visible photons at the ångström thickness limit,” *Nat. Nanotechnol.* **14**, 844–850 (2019).
- ¹⁵ Thomas D Green, Denis G Baranov, Battulga Munkhbat, Ruggero Verre, Timur Shegai, and Mikael Käll, “Optical material anisotropy in high-index transition metal dichalcogenide mie nanoresonators,” *Optica* **7**, 680–686 (2020).
- ¹⁶ Battulga Munkhbat, Denis G Baranov, Michael Stührenberg, Martin Wersäll, Ankit Bisht, and Timur Shegai, “Self-hybridized exciton-polaritons in multilayers of transition metal dichalcogenides for efficient light absorption,” *ACS Photonics* **6**, 139–147 (2018).
- ¹⁷ Lena Yadgarov, Bojana Višić, Tsafrir Abir, Ron Tenne, Alexander Yu Polyakov, Roi Levi, Tatyana V Dolgova, Varvara V Zubuyuk, Andrey A Fedyanin, Eugene A Goodilin, *et al.*, “Strong light–matter interaction in tungsten disulfide nanotubes,” *Phys. Chem. Chem. Phys.* **20**, 20812–20820 (2018).
- ¹⁸ Viktoriia E Babicheva and Jerome V Moloney, “Lattice Resonances in Transdimensional WS₂ Nanoantenna Arrays,” *Appl. Sci.* **9**, 2005 (2019).
- ¹⁹ Sebastian Busschaert, René Reimann, Moritz Cavigelli, Ronja Khelifa, Achint Jain, and Lukas Novotny, “Transition metal dichalcogenide resonators for second harmonic signal enhancement,” *ACS Photonics* **7**, 2482–2488 (2020).
- ²⁰ Mudassar Nauman, Jingshi Yan, Domenico de Ceglia, Mohsen Rahmani, Khosro Zangeneh Kamali, Costantino De Angelis, Andrey E Miroshnichenko, Yuerui Lu, and Dragomir N Neshev, “Tunable unidirectional nonlinear emission from transition-metal-dichalcogenide metasurfaces,” *Nat. Commun.* **12**, 5597 (2021).
- ²¹ HNS Krishnamoorthy, G Adamo, J Yin, V Savinov, NI Zheludev, and C Soci, “Infrared dielectric metamaterials from high refractive index chalcogenides,” *Nat. Commun.* **11**, 1692 (2020).
- ²² Dorte R Danielsen, Anton Lyksborg-Andersen, Kirstine ES Nielsen, Bjarke S Jessen, Timothy J Booth, Manh-Ha Doan, Yingqiu Zhou, Peter Bøggild, and Lene Gammelgaard, “Super-resolution nanolithography of two-dimensional materials by anisotropic etching,” *ACS Appl. Mater. Interfaces* **13**, 41886–41894 (2021).
- ²³ Battulga Munkhbat, Andrew B Yankovich, Ruggero Verre, Eva Olsson, and Timur O Shegai, “Transition metal dichalcogenide metamaterials with atomic precision,” *Nat. Commun.* **11**, 4604 (2020).
- ²⁴ Akash Laturia, Maarten L Van de Put, and William G Vandenberghe, “Dielectric properties of hexagonal boron nitride and transition metal dichalcogenides: from monolayer to bulk,” *npj 2D Mater. Appl.* **2**, 6 (2018).
- ²⁵ Anton A Shubnic, Roman G Polozkov, Ivan A Shelykh, and Ivan V Iorsh, “High refractive index and extreme biaxial optical anisotropy of rhenium diselenide for applications in all-dielectric nanophotonics,” *Nanophotonics* **9**, 4737–4742 (2020).
- ²⁶ Zhengyang Cai, Bilu Liu, Xiaolong Zou, and Hui-Ming Cheng, “Chemical vapor deposition growth and applications of two-dimensional materials and their heterostructures,” *Chem. Rev.* **118**, 6091–6133 (2018).
- ²⁷ Mangesh S Diware, Kyunam Park, Jihun Mun, Han Gyeol Park, Won Chegal, Yong Jai Cho, Hyun Mo Cho, Jusang Park, Hyungjun Kim, Sang-Woo Kang, *et al.*, “Characterization of wafer-scale MoS₂ and WSe₂ 2D films by spectroscopic ellipsometry,” *Curr. Appl. Phys.* **17**, 1329–1334 (2017).
- ²⁸ Ilkka Kylänpää and Hannu-Pekka Komsa, “Binding energies of exciton complexes in transition metal dichalcogenide monolayers and effect of dielectric environment,” *Phys. Rev. B* **92**, 205418 (2015).
- ²⁹ Andres Castellanos-Gomez, Michele Buscema, Rianda Molenaar, Vibhor Singh, Laurens Janssen, Herre S J van der Zant, and Gary A Steele, “Deterministic transfer of two-dimensional materials by all-dry viscoelastic stamp-

- ing,” 2D Mater. **1**, 011002 (2014).
- ³⁰ Kei Kinoshita, Rai Moriya, Momoko Onodera, Yusai Wakafuji, Satoru Masubuchi, Kenji Watanabe, Takashi Taniguchi, and Tomoki Machida, “Dry release transfer of graphene and few-layer h-BN by utilizing thermoplasticity of polypropylene carbonate,” npj 2D Mater. Appl. **3**, 22 (2019).
 - ³¹ Pasqual Rivera, Hongyi Yu, Kyle L Seyler, Nathan P Wilson, Wang Yao, and Xiaodong Xu, “Interlayer valley excitons in heterobilayers of transition metal dichalcogenides,” Nat. Nanotechnol. **13**, 1004–1015 (2018).
 - ³² Chang-Hua Liu, Jiajiu Zheng, Shane Colburn, Taylor K Fryett, Yueyang Chen, Xiaodong Xu, and Arka Majumdar, “Ultrathin van der Waals metalenses,” Nano Lett. **18**, 6961–6966 (2018).
 - ³³ Haonan Ling, Renjie Li, and Artur R Davoyan, “All van der waals integrated nanophotonics with bulk transition metal dichalcogenides,” ACS Photonics **8**, 721–730 (2021).
 - ³⁴ AR Beal, WY Liang, and HP Hughes, “Kramers-Kronig analysis of the reflectivity spectra of 3R-WS₂ and 2H-WSe₂,” J. Phys. C Solid State Phys. **9**, 2449–2457 (1976).
 - ³⁵ AR Beal and HP Hughes, “Kramers-Kronig analysis of the reflectivity spectra of 2H-MoS₂, 2H-MoSe₂ and 2H-MoTe₂,” J. Phys. C Solid State Phys. **12**, 881–890 (1979).
 - ³⁶ Zhenxi Xu, Davide Ferraro, Annamaria Zaltron, Nicola Galvanetto, Alessandro Martucci, Luzhao Sun, Pengfei Yang, Yanfeng Zhang, Yuechen Wang, Zhongfan Liu, *et al.*, “Optical detection of the susceptibility tensor in two-dimensional crystals,” Commun. Phys. **4**, 215 (2021).
 - ³⁷ H.H. Li, “Refractive index of silicon and germanium and its wavelength and temperature derivatives,” J. Phys. Chem. Ref. Data **9**, 561–658 (1980).
 - ³⁸ Daniel T. Pierce and Wo E. Spicer, “Electronic structure of amorphous Si from photoemission and optical studies,” Phys. Rev. B **5**, 3017–3029 (1972).
 - ³⁹ Konstantinos Papatryfonos, Todora Angelova, Antoine Brimont, Barry Reid, Stefan Guldin, Peter Raymond Smith, Mingchu Tang, Keshuang Li, Alwyn J Seeds, Huiyun Liu, *et al.*, “Refractive indices of MBE-grown Al_xGa_(1-x)As ternary alloys in the transparent wavelength region,” AIP Adv. **11**, 025327 (2021).
 - ⁴⁰ Battulga Munkhbat, Betül Küçüköz, Denis G Baranov, Tomasz J Antosiewicz, and Timur O Shegai, “Nanostructured transition metal dichalcogenide multilayers for advanced nanophotonics,” arXiv preprint arXiv:2202.04898 (2022).
 - ⁴¹ Osamu Takayama, Lucian-Cornel Crasovan, Steffen Kjær Johansen, Dumitru Mihalache, David Artigas, and Lluís Torner, “Dyakonov surface waves: A review,” Electromagnetics **28**, 126–145 (2008).
 - ⁴² Osamu Takayama, Lucian Crasovan, David Artigas, and Lluís Torner, “Observation of Dyakonov surface waves,” Phys. Rev. Lett. **102**, 043903 (2009).
 - ⁴³ Osamu Takayama, David Artigas, and Lluís Torner, “Lossless directional guiding of light in dielectric nanosheets using Dyakonov surface waves,” Nat. Nanotechnol. **9**, 419–424 (2014).
 - ⁴⁴ Ozgur Burak Aslan, Daniel A. Chenet, Arend M. Van Der Zande, James C. Hone, and Tony F. Heinz, “Linearly polarized excitons in single- and few-layer ReS₂ crystals,” ACS Photonics **3**, 96–101 (2016).
 - ⁴⁵ Haifeng Wang, Erfu Liu, Yu Wang, Bo Wan, Ching-Hwa Ho, F Miao, and XG Wan, “Cleavage tendency of anisotropic two-dimensional materials: ReX₂ (X=S, Se) and WTe₂,” Phys. Rev. B **96**, 165418 (2017).
 - ⁴⁶ Betül Küçüköz, Battulga Munkhbat, and Timur O Shegai, “Boosting second-harmonic generation in monolayer rhenium disulfide by reversible laser patterning,” ACS Photonics **9**, 518–526 (2022).
 - ⁴⁷ J. N. Hilfiker, N. Singh, T. Tiwald, D. Convey, S. M. Smith, J. H. Baker, and H. G. Tompkins, “Survey of methods to characterize thin absorbing films with spectroscopic ellipsometry,” Thin Solid Films **516**, 7979–7989 (2008).
 - ⁴⁸ Chong Wang, Shenyang Huang, Qiaoxia Xing, Yuangang Xie, Chaoyu Song, Fanjie Wang, and Hugen Yan, “Van der Waals thin films of WTe₂ for natural hyperbolic plasmonic surfaces,” Nat. Commun. **11**, 1158 (2020).
 - ⁴⁹ Hongwei Wang and Tony Low, “Hyperbolicity in two-dimensional transition metal ditellurides induced by electronic bands nesting,” Phys. Rev. B **102**, 241104 (2020).

Supporting Information

Optical constants of several multilayer transition metal dichalcogenides measured by spectroscopic ellipsometry in the 300-1700 nm range: high-index, anisotropy, and hyperbolicity

Battulga Munkhbat,^{1,2,*} Piotr Wróbel,^{3,*} Tomasz J. Antosiewicz,^{3,1,†} and Timur O. Shegai^{1,‡}

¹*Department of Physics, Chalmers University of Technology, 412 96, Gothenburg, Sweden*

²*Department of Photonics Engineering, Technical University of Denmark, 2800 Kongens Lyngby, Denmark*

³*Faculty of Physics, University of Warsaw, Pasteura 5, 02-093 Warsaw, Poland*

**These authors contributed equally to this work.*

[†]*email: tomasz.antosiewicz@fuw.edu.pl*

[‡]*email: timurs@chalmers.se*

Contents

Figures – Examples of raw experimental data and ellipsometric fits	2
Tables of ellipsometric models' parameters	11
S1. Comparison of ellipsometric fitting parameters for uniaxial TMDs	11
S2. Comparison of ellipsometric fitting parameters for bianisotropic TMDs	12
Supporting Notes	12
S1. Uncertainty of optical constants	12

Figures – Examples of raw experimental data and ellipso-metric fits

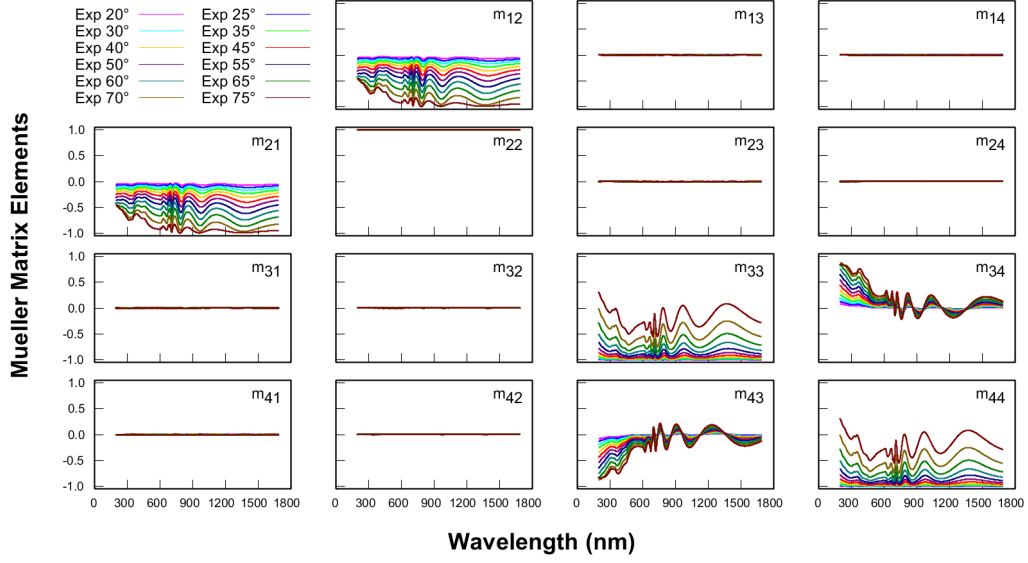


Figure S1: Mueller Matrix elements for a selected MoS₂ flake on a silicon substrate. Note that the zeros in the off-diagonal 2×2 sub-blocks prove the uniaxial nature of this material.

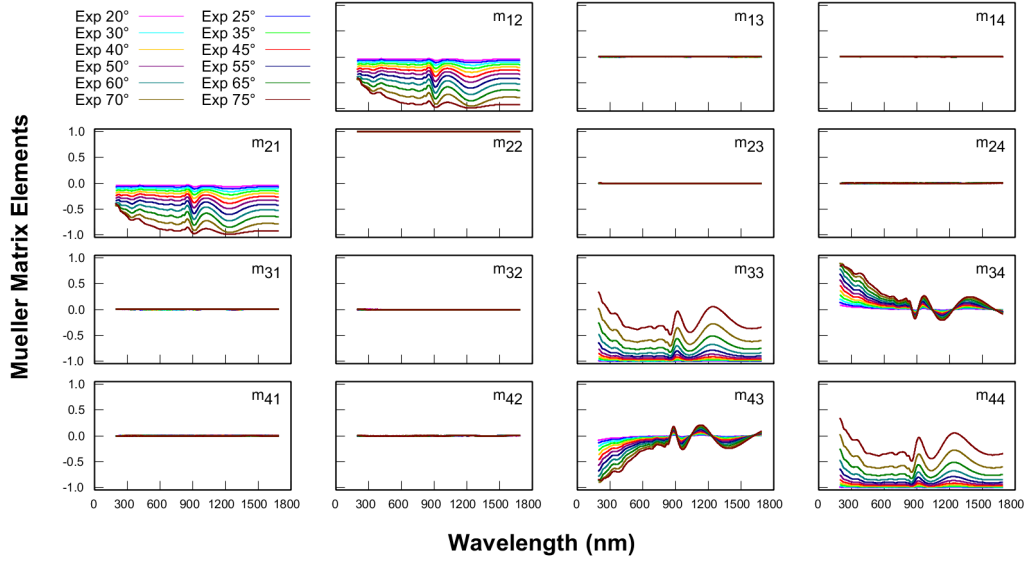


Figure S2: Mueller Matrix elements for a selected MoSe₂ flake on a silicon substrate. Note that the zeros in the off-diagonal 2×2 sub-blocks prove the uniaxial nature of this material.

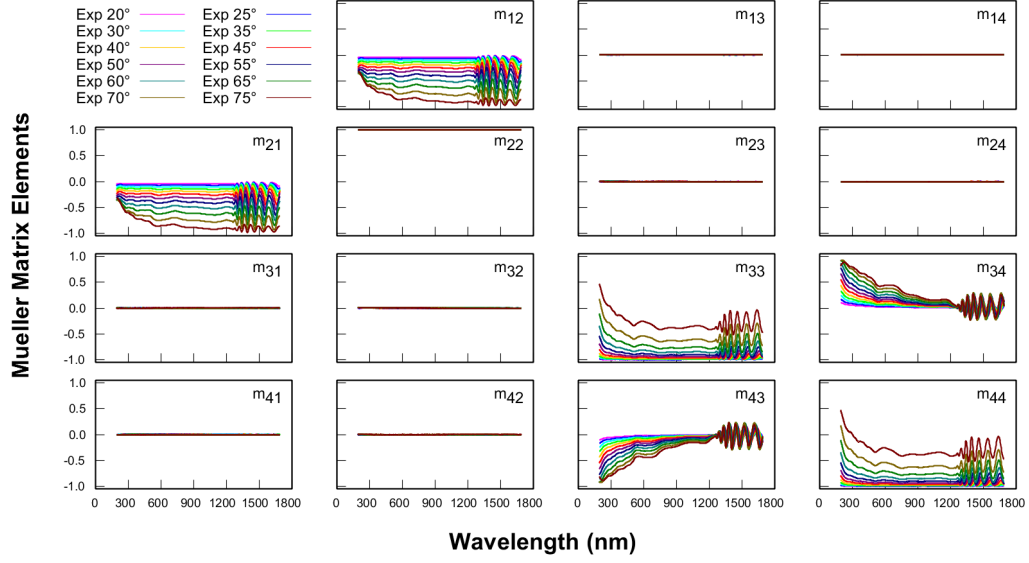


Figure S3: Mueller Matrix elements for a selected MoTe₂ flake on a silicon substrate. Note that the zeros in the off-diagonal 2×2 sub-blocks prove the uniaxial nature of this material.

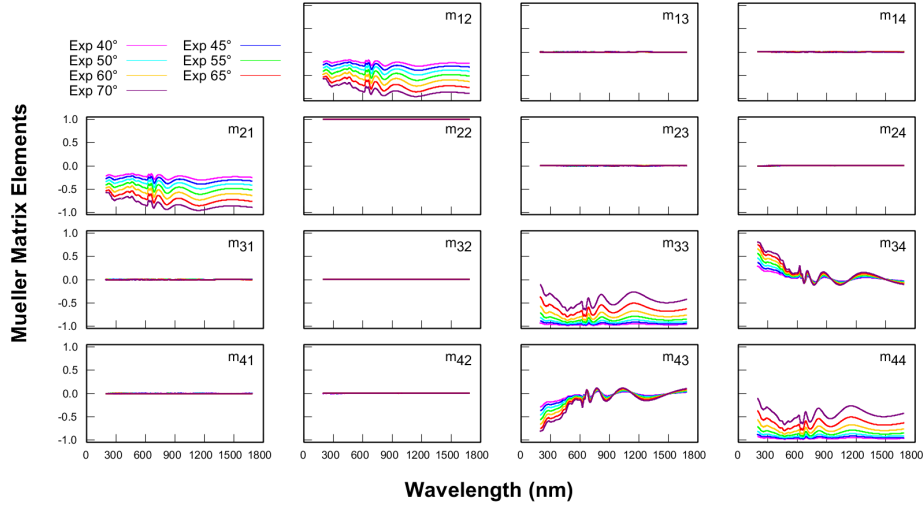


Figure S4: Mueller Matrix elements for a selected WS₂ flake on a silicon substrate. Note that the zeros in the off-diagonal 2×2 sub-blocks prove the uniaxial nature of this material.

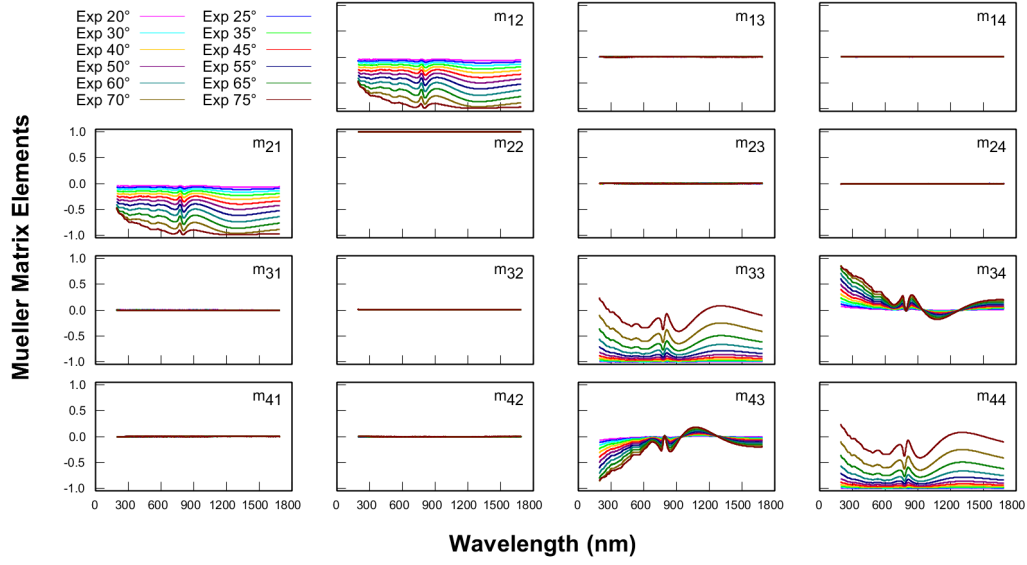


Figure S5: Mueller Matrix elements for a selected WSe₂ flake on a silicon substrate. Note that the zeros in the off-diagonal 2×2 sub-blocks prove the uniaxial nature of this material.

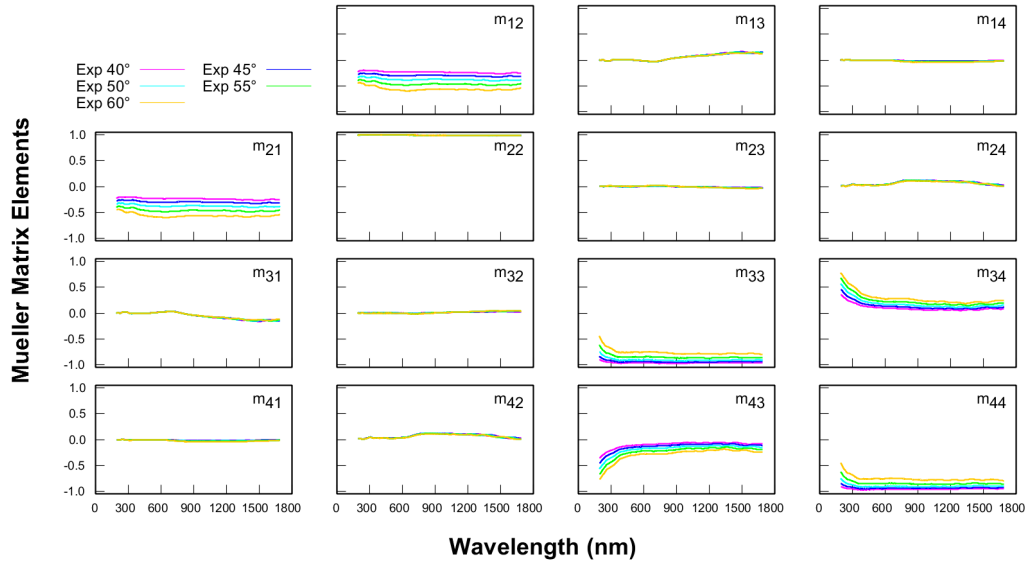


Figure S6: Mueller Matrix elements for a selected WTe₂ flake on a silicon substrate. Note that the off-diagonal 2×2 sub-blocks show the bianisotropic nature of this material.

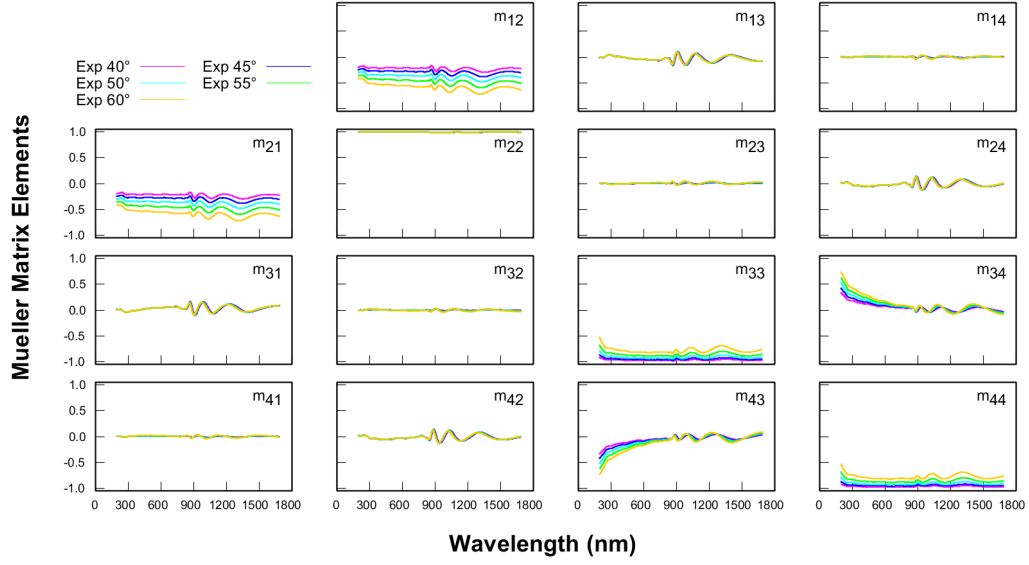


Figure S7: Mueller Matrix elements for a selected ReS_2 flake on a silicon substrate. Note that the off-diagonal 2×2 sub-blocks show the bianisotropic nature of this material.

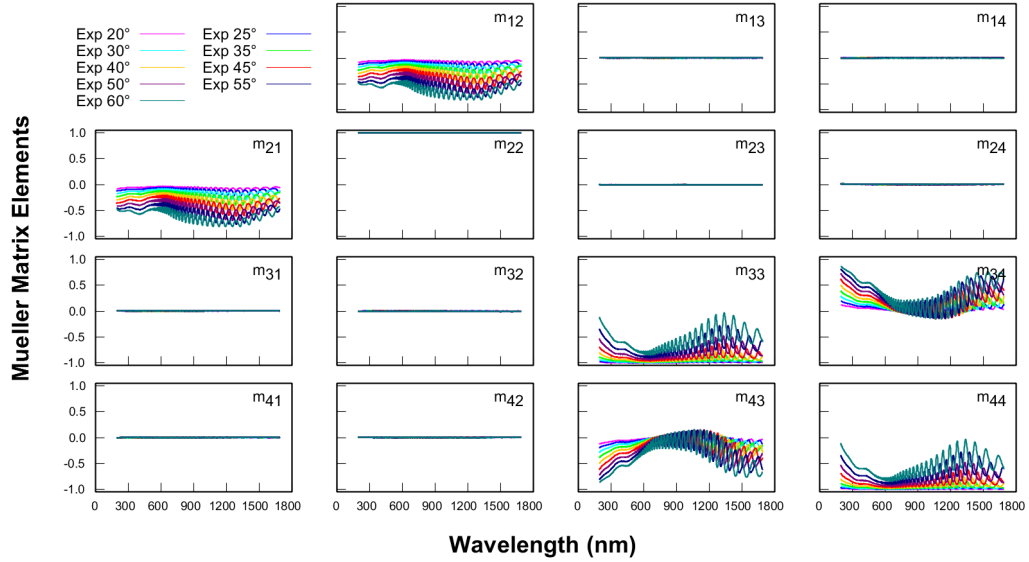


Figure S8: Mueller Matrix elements for a selected NbSe_2 flake on a silicon substrate. Note that the zeros in the off-diagonal 2×2 sub-blocks prove the uniaxial nature of this material.

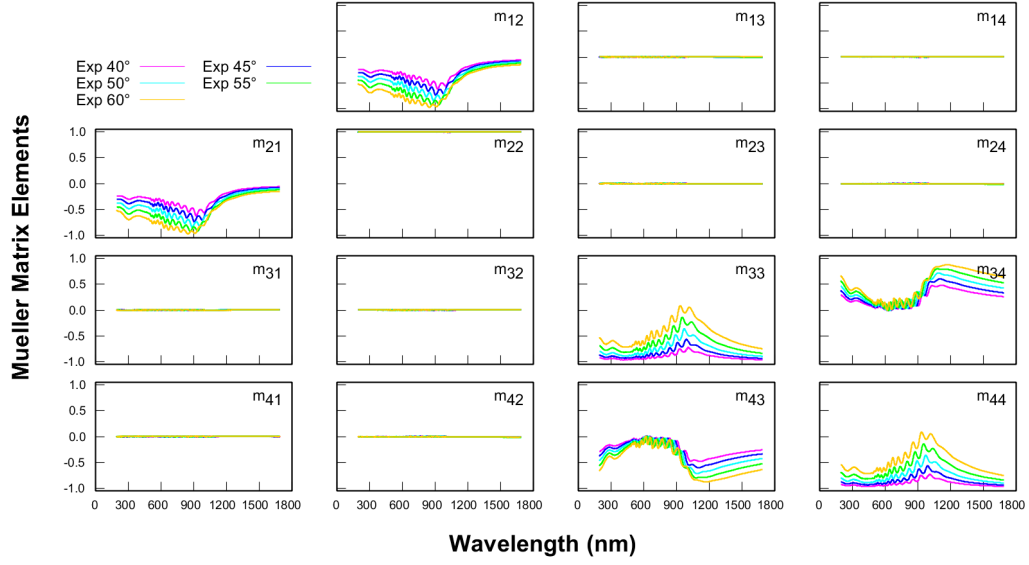


Figure S9: Mueller Matrix elements for a selected TaS₂ flake on a silicon substrate. Note that the zeros in the off-diagonal 2×2 sub-blocks prove the uniaxial nature of this material.

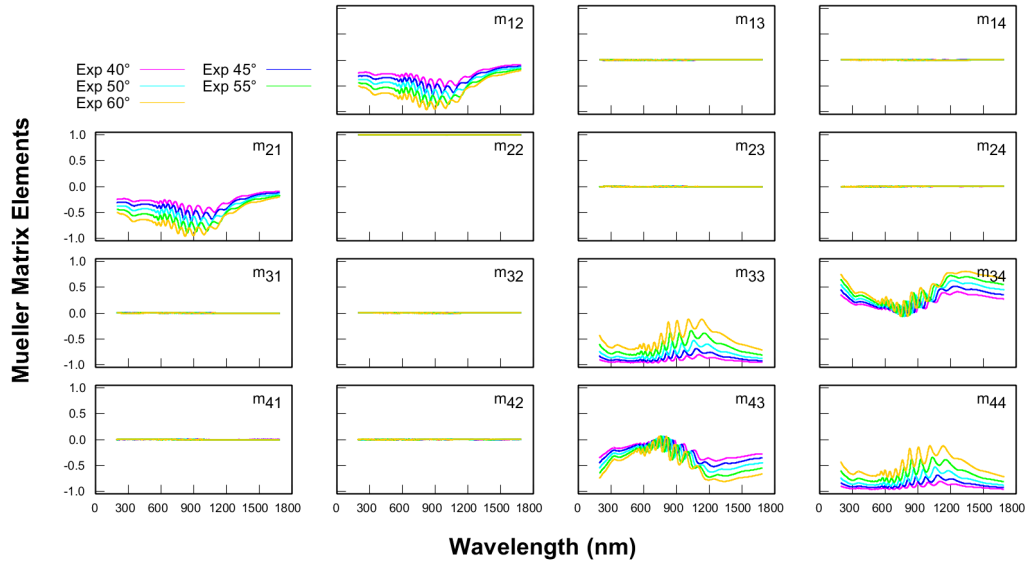


Figure S10: Mueller Matrix elements for a selected TaSe₂ flake on a silicon substrate. Note that the zeros in the off-diagonal 2×2 sub-blocks prove the uniaxial nature of this material.

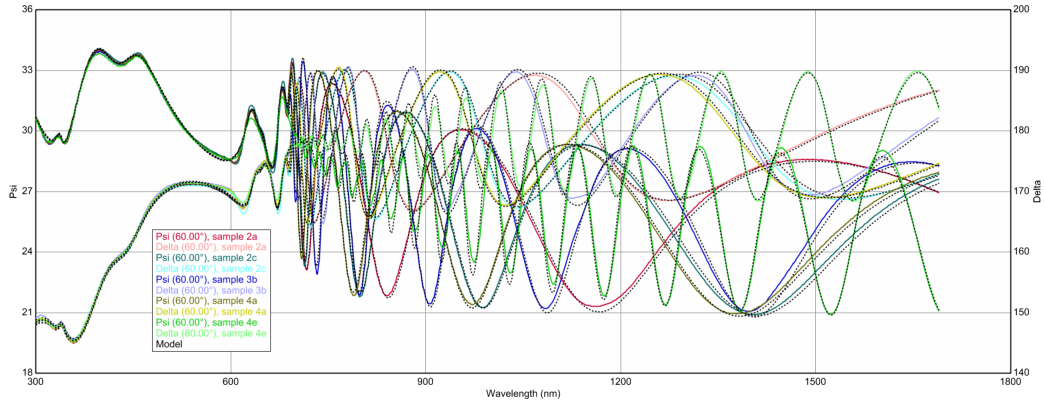


Figure S11: Fidelity of the model fit to measurement data for MoS_2 .

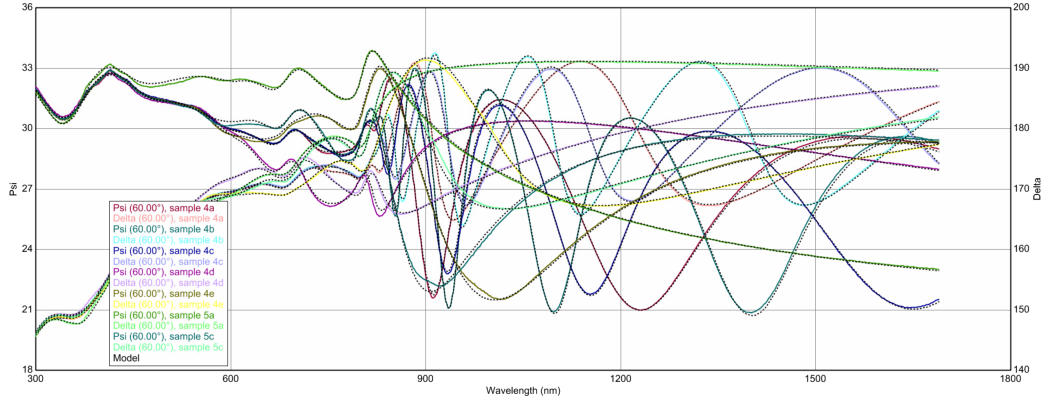


Figure S12: Fidelity of the model fit to measurement data for MoSe_2 .

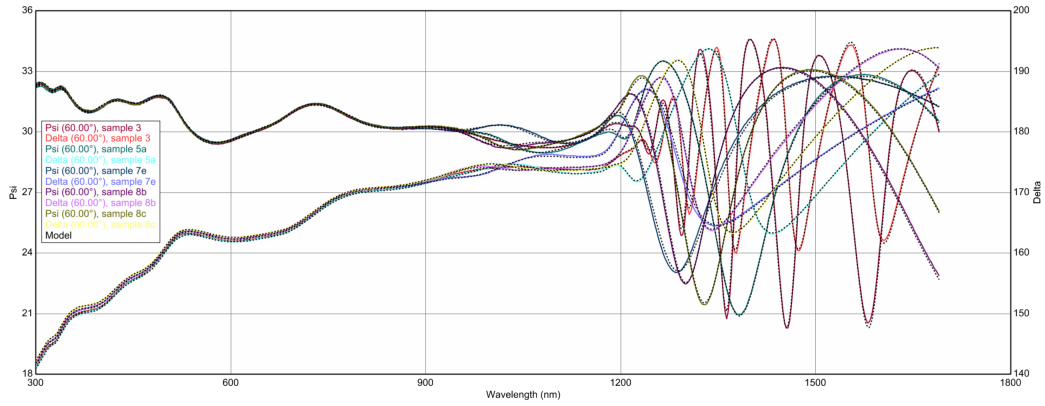


Figure S13: Fidelity of the model fit to measurement data for MoTe_2 .

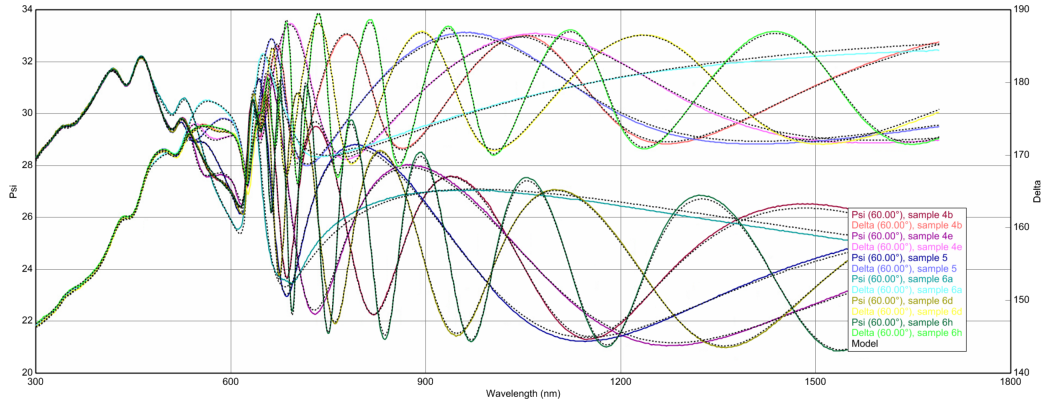


Figure S14: Fidelity of the model fit to measurement data for WS_2 .

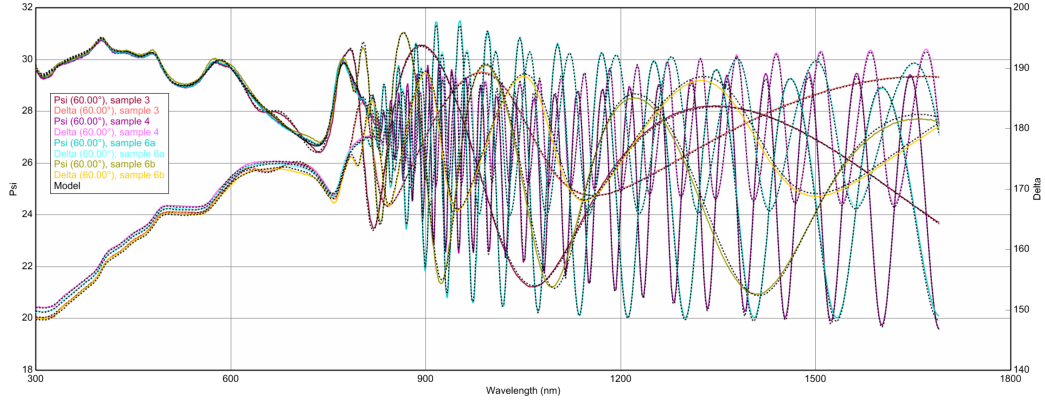


Figure S15: Fidelity of the model fit to measurement data for WSe_2 .

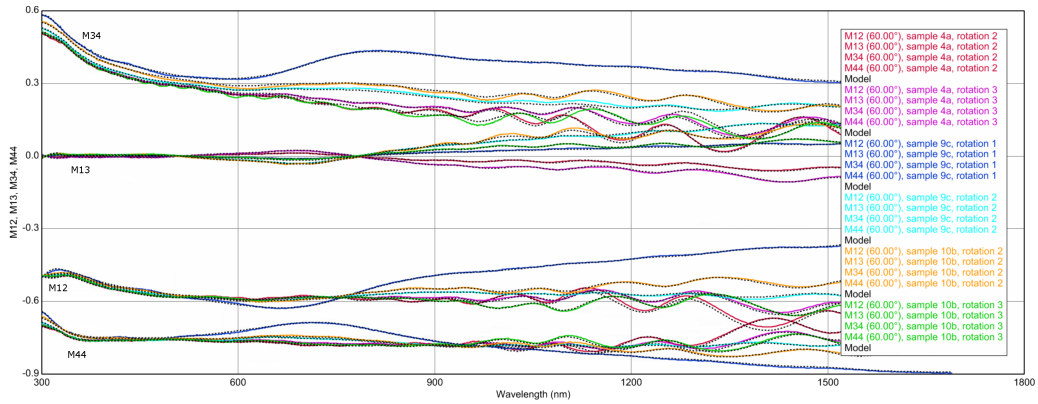


Figure S16: Fidelity of the model fit to measurement data for WTe_2 .

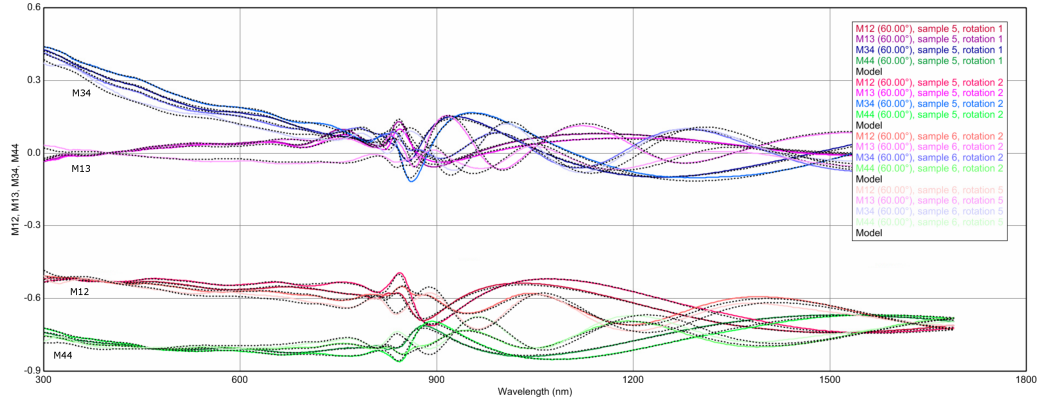


Figure S17: Fidelity of the model fit to measurement data for ReS_2 .

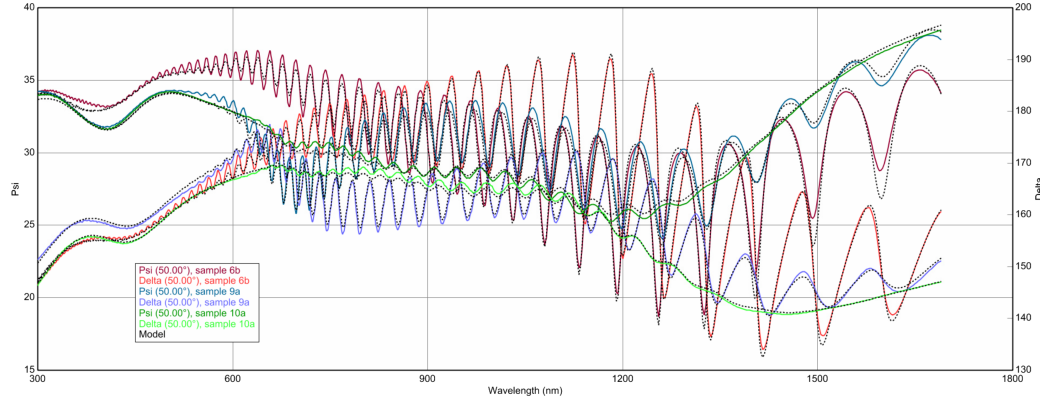


Figure S18: Fidelity of the model fit to measurement data for NbSe_2 .

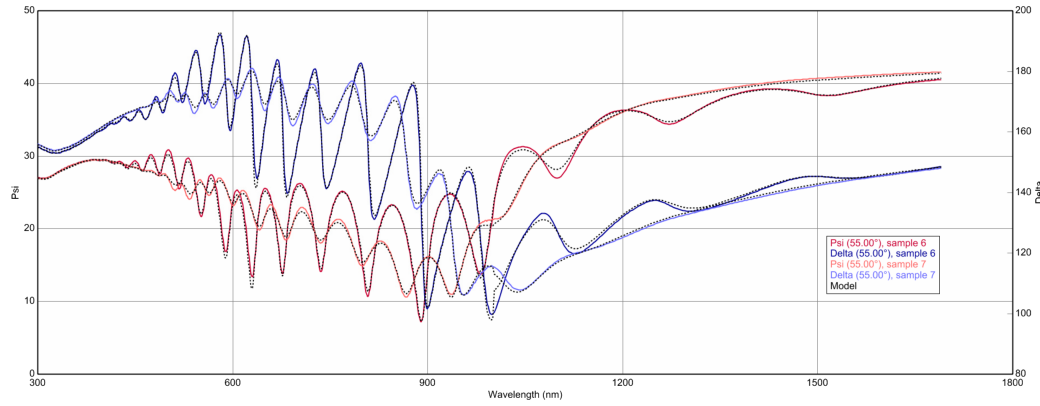


Figure S19: Fidelity of the model fit to measurement data for TaS_2 .

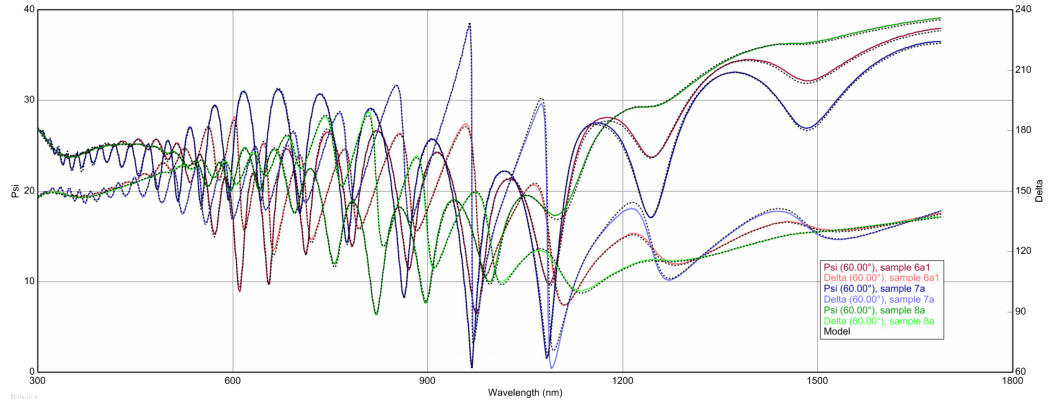


Figure S20: Fidelity of the model fit to measurement data for TaSe₂.

Tables of ellipsometric models' parameters

Table S1: Comparison of ellipsometric fitting parameters for uniaxial TMDs. The fitted thickness values agree very well with (where available) reference thickness measurements obtained with a profilometer.

Material	Sample	Thickness			Roughness (nm)
		reference (nm)	fitted (nm)	nonuniformity (%)	
MoS ₂	2a	301	297	0	1.5
	2c	364	366	0	1.5
	3b	600	546	1.5	1.2
	4a	359	359	0	1.3
	4e	1830	1778	3.4	1.2
MoSe ₂	1	108	113	0	1.2
	2	123	124	0	0.8
	4a	324	301	0	1.2
	4b	538	524	0	1.1
	4c	418	418	7.6	1.1
	4d	75	76	22.4	0.8
	4e	118	118	0	1.3
	5a	24	30	20.2	0.9
	5b	75	77	23.6	2.0
	5c	93	100	0	1.1
MoTe ₂	3	1600	1535	1.5	1.4
	5a	428	430	0	1.5
	7e	259	253	9.2	1.2
	8b	400	388	3.6	1.1
	8c	440	403	0.7	0.9
WS ₂	3a	1140	1165	0	1.2
	3b	454	456	0.1	1.4
	3d	1356	1356	0.1	1.3
	4b	328	325	0	1.4
	4c	2325	2247	0	1.3
	4e	183	184	0	1.5
	5	164	163	0.1	1.5
	6a	91	81	0.1	1.5
	6d	369	389	0	1.5
	6h	660	664	0	1.4
WSe ₂	3	300	273	4.5	1.5
	4	3601	3829	0.3	0.8
	6a	–	2033	0.9	1.1
	6b	613	562	3.2	1.7
NbSe ₂	6b	52	52	0.4	6.1
	9a	122	122	0	3.5
	10a	373	372	0	7.4
TaS ₂	6	120	120	0.5	2.7
	7	250	269	0	2.2
TaSe ₂	6a1	102	102	0	3.3
	7a	74	70	0.7	3.8
	8a	176	173	0.2	3.6

Table S2: Comparison of ellipsometric fitting parameters for bianisotropic TMDs. The fitted thickness values agree very well with (where available) reference thickness measurements obtained with a profilometer, as do the relative rotation angles. [†]Note, that sample 7 of ReS₂ is L-shaped and the two arms have different thicknesses as confirmed by profilometer measurements and ellipsometry fitting.

Material	Sample	Thickness			Roughness (nm)	Orientation angle	
		reference (nm)	fitted (nm)	nonuniformity (%)		reference (degrees)	fitted (degrees)
ReS ₂	5	196	203	1.2	1.5	-1.6	35.8
			208	2.7	1.6	-16.2	21.8
	6	483	483	2.5	1.6	15.3	46.4
			512	2.9	1.8	81.2	110.4
	7 [†]	191	190	0.5	1.4	-22.3	-7.7
			681	5.9	1.8	42.3	57.7
WTe ₂	4a	256	233	0.9	0.2	19.6	10.7
			251	3.4	0.2	31.1	22.0
			235	1.9	0.4	46.0	37.9
	5	410	403	1.3	0.3	-1.5	-86.3
			417	1.6	0.5	41.5	-41.7
			460	1.6	0.4	62.8	-20.2
	9c	440	397	1.1	0.4	0.8	-80.4
			412	1.9	0.3	46.3	-35.0
			372	6.6	0.3	86.6	6.1
	10b	233	279	0.4	0.7	45.1	-40.4
			272	1.5	0.2	73.0	-15.3

Supporting Notes

Supporting Note S1: Uncertainty of optical constants.

Evaluation of inaccuracies of extracting the optical parameters from ellipsometric measurements is a very challenging task and cannot be done unequivocally, since the technique is not a direct method. The uncertainty can be influenced by systematic errors of the measurement itself like beam divergence, angle of incidence, sample position, etc, however, the biggest impact on the trustworthiness of the extracted data stems from the optical model. Its validity can be judged by the fit quality and statistically by the Mean Squared Error (MSE), which is a prime parameter used for evaluating the model and how it fits the measured data. However, the MSE parameter alone is merely an indicator that in the case of yielding small values the model might be true. More importantly, it does not take into account what is the sensitivity of the model to the various fitting parameters.

Thus, another way to evaluate the model is the uniqueness test. In this test of the model a given parameter, for example the layer thickness, is fixed (in a given range) at various values while all the other ones are fitted. The width (or more generally the shape) of the minimum of the MSE curve as a function of the chosen parameter shows the uncertainty of the model. However, considering the fact that many parameters of the model influence the final result and their impact may be vary depending on a particular spectral range, using this measure alone for the evaluation of uncertainties of optical constants may be insufficient as well.

A more systematic way of evaluating the goodness of the proposed models and their fits is done using a Fit Parameter Error Estimation tool that is included in the analysis software (CompleteEASE). (i) The first procedure is based on analyzing random errors to show the influence of the measurement uncertainties. It reanalyzes a randomized set of trial experimental

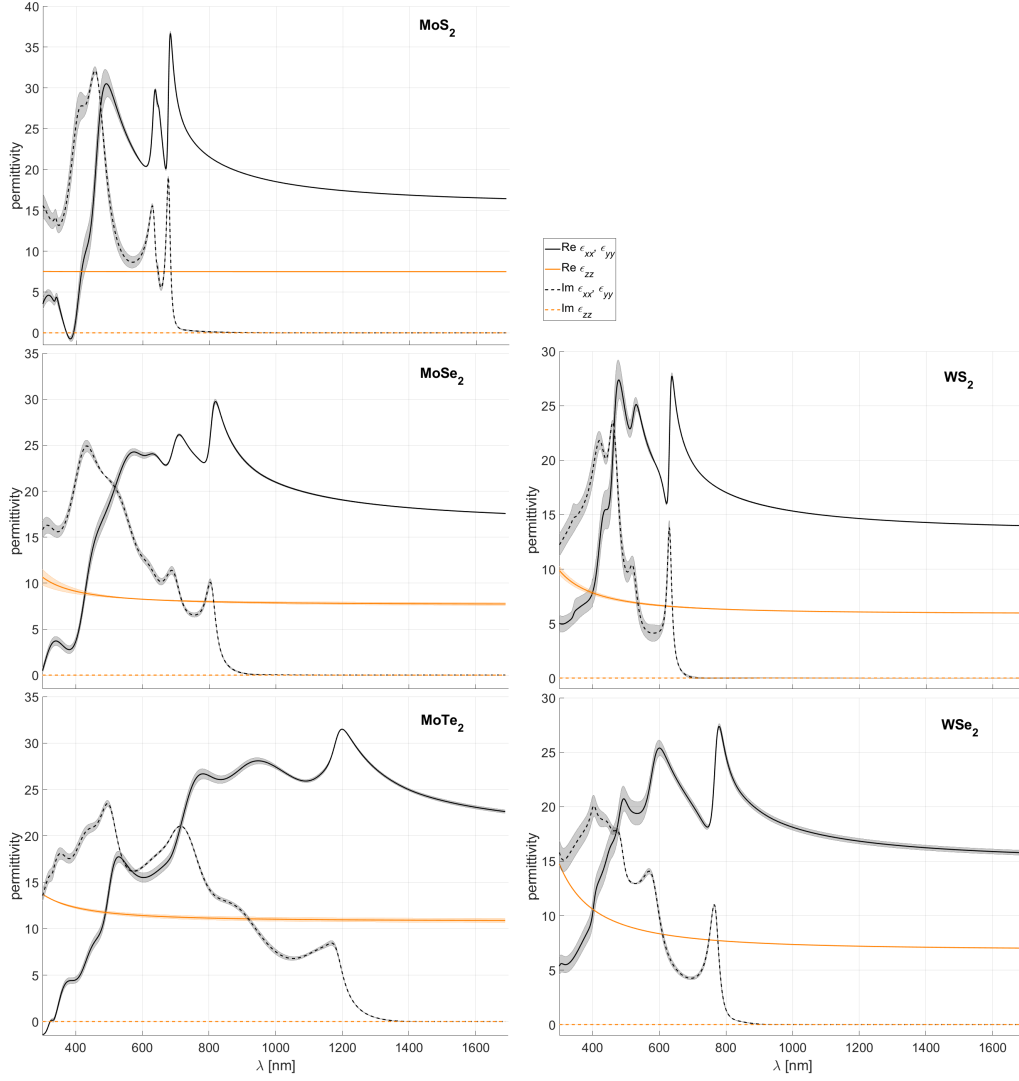


Figure S21: Uncertainty of the complex permittivity for uniaxial semitransparent TMDCs.

data based on the original measurements and refits many sets with the same model. This gives an estimate of the uncertainty for individual fitting parameters as well as the optical constants. (ii) Another set of procedures evaluates the influence of systematic errors coming from such sources as angle offset, wavelength shift, Ψ , and Δ offset or inaccuracies of the complex refractive index of the substrate. (iii) Finally, magnitudes of the fitting errors are tested by adding or subtracting the same magnitude of error at every wavelength to the existing data set and refitting the manipulated data.

Our analysis shows that both random and systematic errors (tested as described above) give a minor contribution to the overall uncertainty of the dielectric functions. On the other hand, the magnitude of the fit error shows the largest influence on the models' spectral sensitivity comes from the distinct optical properties of the subsequent materials. For uniaxial semitransparent TMDs the permittivity errors shown in [Figure S21](#) are negligible in the transparent regions and increase for shorter wavelengths in the absorption bands. This is a result of a lower sensitivity of ellipsometry (the method) itself due to high absorbance in the materials and an influence of the surface roughness, which plays an important role in determining the optical properties of the materials, especially in the UV region.

In the case of bi-anisotropic materials (see [Figure S22](#)), ReS_2 shows similar properties in terms of uncertainties of optical parameters to the above examples, as it is also transparent at long wavelengths. In contrast, WTe_2 exhibits comparatively larger errorbars with an increase of the wavelength for the in-plane components and a pronounced uncertainty for the out-of-plane

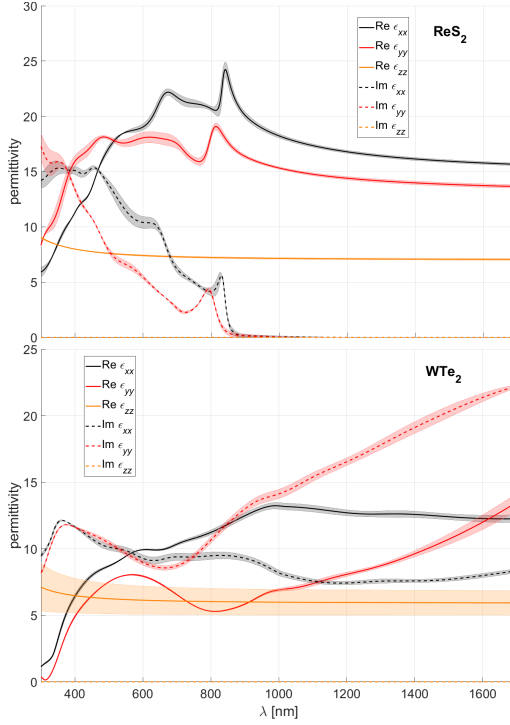


Figure S22: Uncertainty of the complex permittivity for bi-anisotropic TMDCs.

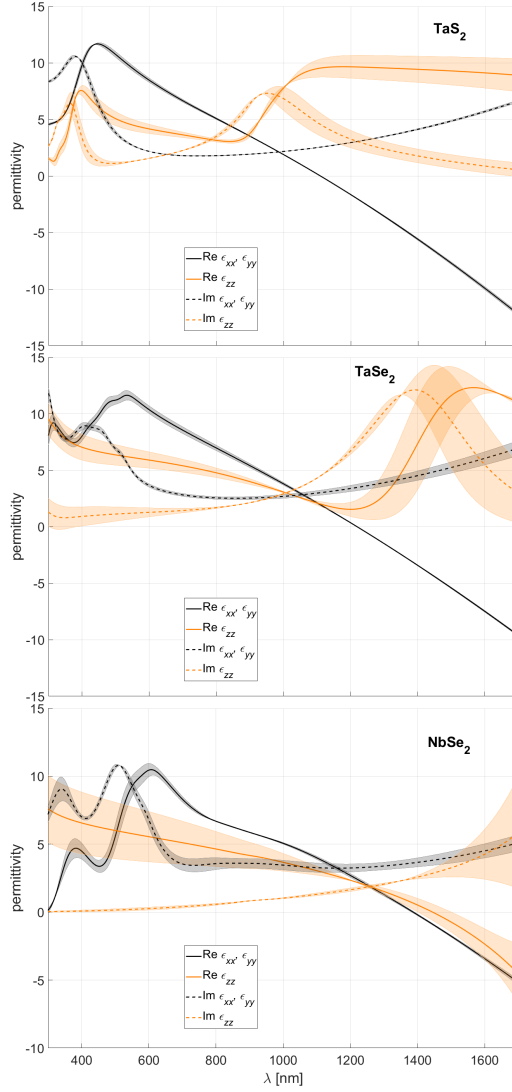


Figure S23: Uncertainty of the complex permittivity for metallic TMDCs.

component in the entire spectral region. The latter one is attributed to the overall large absorptivity of the material in the whole spectral range. This was partially mitigated by preparation of only thin samples, however, due to the mechanical properties of WTe_2 we were only able to obtain flakes with thicknesses down to ~ 200 nm. Unfortunately, ca. 200 nm WTe_2 flakes still absorb a significant amount of light. Thus, the measured ellipsometric curves lack clear and deep interference features despite a SiO_2 layer between the WTe_2 flakes and the Si substrate. These limitations of preparing WTe_2 flakes led to a low sensitivity of the model to the ϵ_{zz} component.

Metallic TMDs show enhanced errorbars in the spectral regions with high absorptivity, as illustrated in Figure S23, resulting in a decrease of the interferometric spectral features – see Figure S8–Figure S10 – which leads to high uncertainty of out-of-plane components. It is important to stress that this analysis does not evaluate the overall uncertainty of the ellipsometric technique but rather shows the sensitivity of the models resulting from unique material properties of subsequent samples